As of 10 June 2016

This GOES-R Level 2+ space weather Algorithm Theoretical Basis Document (ATBD) is preliminary and subject to change as the GOES-R Program prepares for a launch in late 2016.

The NOAA National Centers for Environmental Information (NCEI) is currently developing a demonstration version of the Satellite Product Analysis and Distribution Enterprise System (SPADES) which will host the L2+ algorithms. The operational SPADES will be instantiated by the National Weather Service in FY2017 to serve the needs of the Space Weather Prediction Center (SWPC).

Updated versions of the L2+ ATBDs will periodically be made available and posted to the SPADES website.

Bill Denig
NCEI

http://www.ngdc.noaa.gov/stp/space-weather/online-publications/stp_sii/spades/

NOAA NESDIS
National Centers for Environmental Information

GOES-R SEISS.19
DENSITY AND TEMPERATURE MOMENTS AND LEVEL OF SPACECRAFT CHARGING ALGORITHM THEORETICAL BASIS DOCUMENT
Version 1.2

Hardcopy Uncontrolled

TITLE: SEISS.19 DENSITY AND TEMPERATURE MOMENTS AND LEVEL OF SPACECRAFT CHARGING ALGORITHM THEORETICAL BASIS DOCUMENT

AUTHORS:
Juan V. Rodriguez

APPROVAL SIGNATURES:

<Actual Signature Date>

Brian Kress Date
SEISS Instrument Scientist

<Actual Signature Date>

William Denig Date
NCEI Principal Investigator

<Actual Signature Date>

Steven Goodman Date
GOES-R Chief Scientist

SEISS.19 DENSITY AND TEMPERATURE MOMENTS AND LEVEL OF SPACECRAFT CHARGING ALGORITHM THEORETICAL BASIS DOCUMENT VERSION HISTORY SUMMARY

Version Number	**Date**	**Authors**	**Revision Description**	**Reason for Revision**
1.0	Feb.21, 2011	Juan V. Rodriguez	Initial release	Review
1.1	May 10, 2011	Juan V. Rodriguez	Corrections and clarifications	Code demonstration
1.2	February 18, 2016	Juan V. Rodriguez	Update details based on 5 years of flight and ground segment development. Add some missing theory. Restrict all P3I to section 6 to avoid confusion.	Version for implementation in SPADES

LIST OF FIGURES 9
LIST OF TABLES 11
LIST OF ACRONYMS 12
ABSTRACT 13
1.0 INTRODUCTION 14
1.1 Purpose of This Document 14
1.2 Who Should Use This Document 14
1.3 Inside Each Section 14
1.4 Related Documents 15
1.5 Revision History 15
2.0 OBSERVING SYSTEM OVERVIEW 16
2.1 Product Generated 16
2.2 Instrument Characteristics 16
3.0 ALGORITHM DESCRIPTION 17
3.1 Algorithm Overview 17
3.2 Processing Outline 17
3.3 Algorithm Input 22
3.3.1 Sensor Data 22
3.3.2 Sensor Characterization Data 24
3.4 Theoretical Description 26
3.4.1 Physics of the Problem 26
3.4.2 Mathematical Description 31
3.5 Algorithm Output 42
4.0 TEST DATA SETS AND OUTPUTS 45
4.1 Simulated/Proxy Input Data Sets 45
4.2 Output from Simulated/Proxy Inputs Data Sets including Error Estimates 45
5.0 PRACTICAL CONSIDERATIONS 60
5.1 Numerical Computation Considerations 60
5.2 Programming and Procedural Considerations 61
5.3 Quality Assessment and Diagnostics 61
5.4 Exception Handling 61
5.5 Algorithm Validation 61
6.0 ASSUMPTIONS AND LIMITATIONS 62
6.1 Performance 62
6.2 Assumed Sensor Performance 62
6.3 Pre-Planned Product Improvements (P3I) 63
6.3.1 Validation of Spacecraft Potential Estimate based on Temperature 63
6.3.2 Deriving Field-Aligned Flow Velocity in the Magnetosheath 64
6.3.3 Estimating Cold Ion Density from the Ion Line 64
6.3.4 Combined Partial Moments 64
7.0 REFERENCES 65
APPENDIX A. OVERVIEW OF PARTICLE DISTRIBUTIONS 68

APPENDIX B. EVALUATION OF MOMENTS FOR MAXWELLIAN DISTRIBUTIONS 70
APPENDIX C. DERIVATION OF MOMENTUM TERMS IN RELATIVISTIC TEMPERATURE SOLUTION 73

LIST OF FIGURES

Figure 1. Top-level flow diagram for the MPS-HI Moments algorithm. 18
Figure 2. Top-level flow diagram for the MPS-LO Moments and Level of Spacecraft Charging algorithm. 21
Figure 3. Spectrograms of spin-averaged electron and ion energy differential fluxes measured by the LANL MPA instrument on 2 November 2003. The horizontal axis represents universal time. The vertical axis represents the energies of the particles in electron volts (eV). The color scale represents the base-10 logarithm of the energy flux in units of eV cm^{-2} s^{-1} sr^{-1} eV^{-1}. Examples of trapped secondary and photoelectrons and the ion line can be observed in the fluxes after 1700 UT. The dark blue traces represent the identification by the algorithm of the frame potential and barrier potential. MPA data provided courtesy of M. Thomsen, Los Alamos National Laboratory. 29
Figure 4. An example of spin-averaged ion and electron spectra from the LANL-02A MPA on 2 November 2003, 1950:15 UT. Based on these data, the barrier potential is estimated to be -150 eV and the spacecraft frame potential is estimated to be -700 V. MPA data provided courtesy of M. Thomsen, Los Alamos National Laboratory. 30
Figure 5. Spacecraft potential vs. average electron temperature from three geosynchronous satellites (1994-084, LANL-97A, LANL-02A) in September 2002. Separate fits to eclipse and non-eclipse conditions are shown. Figure courtesy of M. Thomsen, Los Alamos National Laboratory. 31
Figure 6. (Top) The function g(β) as a function of β. The non-relativistic equivalent is plotted with a dashed line. (Middle) The ratio of g(β) to its non-relativistic equivalent. (Bottom) Temperature kT as a function of g(β) (solid line), and the quadratic fit to this expression in log-log space (red dotted line). 39
Figure 7. Spectrograms of (top) electron and (bottom) ion number differential fluxes measured by SSJ/4 on DMSP F7, 24 December 1983, 1341-1344 UT. 47
Figure 8. Density and temperature moments from the DMSP flux measurements shown in Figure 7. The dotted lines represent moments calculated from two-parameter Maxwellian fits to the spectra, and the green lines represent the moments calculated using the integrals. 49
Figure 9. Sample spectra from 1342:00 UT (ions) and 1343:08 (electrons and ions) showing measured velocity distributions (white) and two-parameter Maxwellian fits to these distributions (red). 50
Figure 10. Spectrograms of spin-averaged electron and ion energy differential fluxes measured by the LANL MPA instrument on 26 October 2003. The horizontal axis represents universal time. The vertical axis represents the energies of the particles in electron volts (eV). The color scale represents the base-10 logarithm of the energy flux in units of eV cm^{-2} s^{-1} sr^{-1} eV^{-1}. MPA data provided courtesy of M. Thomsen, Los Alamos National Laboratory. 51
Figure 11. Ion and electron symmetry axes derived from LANL-02A MPA fluxes measured on 26 October 2003, and the proxy pitch angles derived from them. In the top and middle panel, the white trace indicates the symmetry axis for the given species and

the green trace indicates the 'best' symmetry axis determined by taking the axis with the lowest variance in a 10-sample (~860 s) period. 52
Figure 12. Ion moments from LANL-02A MPA, 26 October 2003. The black traces are the moments from the CDF file, calculated by LANL. The orange traces represent the moments calculated from proxy data with MPA energy resolution and MPS-LO angular resolution. The gree traces represent the moments calculated from proxy data with MPS-LO energy and angular resolution. The numbers at the upper right of each panel represent the lower quartile, median and upper quartile of the absolute differences between the LANL moments and the proxy moments (color-coded)..... 54
Figure 13. Electron moments from LANL-02A MPA, 26 October 2003. The black traces are the moments from the CDF file, calculated by LANL. The orange traces represent the moments calculated from proxy data with MPA energy resolution and MPS-LO angular resolution. The gree traces represent the moments calculated from proxy data with MPS-LO energy and angular resolution. The numbers at the upper right of each panel represent the lower quartile, median and upper quartile of the absolute differences between the LANL moments and the proxy moments (color-coded)..... 55
Figure 14. Spin-averaged ion and electron differential energy flux spectra from 26 October 2003, 1211:56 UT. The white diamonds represent the MPA data and the green asterisks represent the subsampled proxy data. Note that energy flux is a scaling of number flux that is linear with energy. Therefore, the highest energies are emphasized in energy flux. 56
Figure 15. Estimates of spacecraft charging on LANL-02A from 2 November 2003 (see Figure 3 for the spectrogram of the fluxes). The upper panel shows the barrier potential calculated from the electron fluxes. The green trace is at MPA energy resolution and the blue trace is at MPS-LO energy resolution. The lower panel shows the negative of the frame potential derived from the ion data or from the electron temperature moment. The blue diamonds represent the potential derived from the ion line in the proxy data. The green triangles represent the potential derived from the electron temperature from the proxy data. The red line represents the potential from the LANL CDF file..... 57
Figure 16. GOES 14 magnetometer (top panel) and EPEAD electron integral flux (2nd panel) measurements from 6-11 April 2010. The third panel shows the differential fluxes fit to the integral flux using a sum of relativistic Maxwellian, power law, and energy exponential analytical forms, whose weights are shown in the fourth panel. The partial number density and temperature from the relativistic Maxwellian fit (solid lines) and the moments integrals (dotted lines) are shown in the fourth panel. The bottom panel shows the phase space density at fixed values of the first adiabatic invariant. 59

LIST OF TABLES

Table 1. MPS-LO inputs to moments and spacecraft charging algorithm..... 23
Table 2. MPS-HI inputs to moments algorithm..... 24
Table 3. MAG inputs to moments and spacecraft charging algorithms. 24
Table 4. Sensor characterization data used by Moments algorithms. All of these data reside in files with standardized names that are distinguished by version number. 25
Table 5. Values of the constants used in the empirical relation between electron temperature and spacecraft potential. These values will need to be reevaluated for each GOES-R+ satellite. 35
Table 6. Level 2 Outputs (including Quality Flags) of SEISS MPS-LO Moments and Level of Spacecraft Charging Algorithm..... 42
Table 7. Level 2 Outputs (including Quality Flags) of SEISS MPS-HI Moments Algorithm..... 43
Table 8. Comparison of moments calculation for an isotropic Maxwellian of n = 1000 cm^{-3} and a range of temperatures, using two quadrature methods..... 46
Table 9. Units of selected physical quantities used in the Moments algorithm..... 60

LIST OF ACRONYMS

ATBD	Algorithm Theoretical Basis Document
ATS	Applied Technology Satellites
CIRES	Cooperative Institute for Research in Environmental Sciences
DMSP	Defense Meteorological Satellite Program
EPEAD	Energetic Proton, Electron and Alpha Detector (GOES 13-15)
EXIS	EUV and X-Ray Irradiance Sensors
FOV	Field-of-view
LANL	Los Alamos National Laboratory
MAG	GOES Magnetometer
MAGED	Magnetospheric Electron Detector (GOES 13-15)
MAGPD	Magnetospheric Proton Detector (GOES 13-15)
MPA	Magnetospheric Plasma Analyzer
MPS	Magnetospheric Particle Sensor
NASCAP	NASA/Air Force Spacecraft Charging Analyzer Program
PAD	Pitch-angle distribution
P3I	Pre-planned product improvement
SEISS	Space Environment In-Situ Suite
SSJ	Special Sensor J
SWPC	Space Weather Prediction Center
TBR	To be resolved

ABSTRACT

The SEISS Level 2 Density and Temperature Moments and Level of Spacecraft Charging algorithm calculates the densities and temperatures of electrons and ions/protons from 1-minute averages of Magnetospheric Particle Sensor (MPS) fluxes. Densities and temperatures are calculated over three energy ranges, one covered by MPS-LO and two covered by MPS-HI. Two temperatures per energy range are provided, one of the distribution perpendicular to the Earth's magnetic field, and one of the distribution parallel to the field. A measure of the particle distribution anisotropy is calculated from the parallel and perpendicular temperatures. The algorithm uses measurements from the GOES-R+ Magnetometer to calculate the time-varying pitch angles of the particles measured by each telescope/zone. It estimates the pitch angle distribution on a regular grid by accounting for the finite angular response of the telescopes/zones. The algorithm also identifies electron and ion signatures of spacecraft surface (frame) charging in the the MPS-LO fluxes. From these observations, or, in the absence of clear signatures, from the electron temperature, it estimates the spacecraft charging voltage and uses this to correct the measured MPS-LO spectra for the effective change in particle energy prior to calculating the moments. This document describes the theoretical basis of the algorithm; the exception handling built in to the algorithm; the inputs, outputs and data flow; and assumptions and limitations.

1.0 INTRODUCTION

1.1 Purpose of This Document

The purpose of this document is to describe the SEISS Level 2 algorithm that calculates density and temperature moments from 1-minute averages of Magnetospheric Particle Sensor (MPS) electron and ion/proton measurements, and estimates the level of spacecraft surface (frame) charging from MPS-LO measurements. It provides the operational requirements for this Level 2 product and defines how these requirements are met with this algorithm. The algorithm inputs, processing steps, and outputs are described in sufficient detail to support the design, development, testing, validation and implementation of the algorithm in the final operational processing system.

1.2 Who Should Use This Document

All scientific and operational users of the product, both within and outside NOAA, should study this ATBD in order to understand the meaning of the product and the strengths and limitations of the algorithm.

1.3 Inside Each Section

Section 2.0 OBSERVING SYSTEM OVERVIEW:
Describes the SEISS MPS and MAG instruments and the measurements that serve as input to the algorithm.

Section 3.0 ALGORITHM DESCRIPTION:
Describes the development, theory and mathematics of the algorithm. Describes the logical flow of the algorithm, including input and output flow.

Section 4.0 TEST DATA SETS AND OUTPUTS:
Describes the test data sets used to characterize the performance of the algorithm and the data product quality. Describes the results from the algorithm processing on simulated input data.

Section 5.0 PRACTICAL CONSIDERATIONS:
Discusses issues involving numerical computation, programming and procedures, quality assessment and diagnostics and exception handling.

Section 6.0 ASSUMPTIONS AND LIMITATIONS:
Describes assumptions regarding input data contents and formats; instrument performance and characterization data; and potential future changes and improvements.

Section 7.0 REFERENCES:
Provides all references mentioned in the ATBD.

1.4 Related Documents

GOES-R Series Mission Requirements Document (MRD), P417-R-MRD-0070, Version 3.1, December 5, 2007.

Space Environment In-Situ Suite (SEISS) Performance and Operational Requirements Document (PORD), 417-R-SEISSPORD-0030, Baseline Version 2.0, November 16, 2005.

1.5 Revision History

See p. 5

2.0 OBSERVING SYSTEM OVERVIEW

2.1 Product Generated

The SEISS Density and Temperature Moments and Level of Spacecraft Charging algorithm produces partial moments (number densities and parallel and perpendicular temperatures) of electrons and ions/protons in three energy ranges: 0.03-30 keV, 50-700 keV, and 700-4000 keV. It also produces an estimate of the level of spacecraft surface (frame) charging and (when observed) the barrier potential that is trapping locally generated electrons. An anisotropy measure is calculated for each species in each energy range as well.

Although they are intermediate products, the central pitch angles for all zones and telescopes are preserved in the output since they are important to the user community. Quality flags are also provided.

2.2 Instrument Characteristics

The SEISS is the primary instrument and the Magnetometer is the secondary instrument for this product. It is an MRD requirement that the SEISS be located on a satellite with a magnetometer; the Moments algorithm provides part of the rationale for this requirement.

The SEISS operational requirements and characteristics are detailed in the GOES-R Series Mission Requirements Document (MRD, P417-R-MRD-0070) and the SEISS Performance and Operational Requirements Document (PORD, 417-R-SEISSPORD-0030). The requirements pertaining specifically to magnetospheric electrons and protons, which are pertinent to the Moments algorithm, are specified in sections 3.3.6.1.2, 3.3.6.1.3, and 3.4.5 of the MRD and sections 3.2.2 and 3.2.5 of the PORD.

Further description of the instruments is not possible at this time because the information may be restricted under Non-Disclosure Agreements.

3.0 ALGORITHM DESCRIPTION

3.1 Algorithm Overview

The basic rationale for calculating moments of a particle distribution is to reduce tens or hundreds of flux measurements to a few parameters that are useful in practical applications. In a bi-Maxwellian distribution with zero drift velocity, three parameters (number density and the temperatures perpendicular and parallel to the magnetic field) specify the distribution completely (see Appendix A). Maxwellians are in general only approximations (and usually poor approximations) to actual distributions measured in space. However, the number density and equivalent temperatures for a measured distribution can still be calculated using moment integrals over the distribution.

There are applications in which the particle distribution is desired rather than moments. In these cases, the pitch angles will be needed by users of the particle distributions. These intermediate products of the moments algorithm are preserved as L2 outputs.

Due to practical measurement limitations, moments are restricted to portions of the full energy spectrum of particles in space, and therefore are in reality 'partial moments.' This algorithm in fact calculates three sets of partial moments corresponding to three energy ranges. Most users will want to have the separate partial moments and may only use one of the sets. In principle, it is straightforward to combine partial moments (see section 6), though this is currently not done by the operational algorithm due to anticipated difficulties (e.g., intercalibration discrepancies and H+/O+ mix in MPS-LO vs H+ only in MPS-HI) that can only be addressed in the post-launch validation phase.

3.2 Processing Outline

Separate outlines are provided for the MPS-HI and MPS-LO algorithms.

The top-level processing flow for the MPS-HI algorithm is shown in Figure 1. At this level there are no branches or iterative loops.

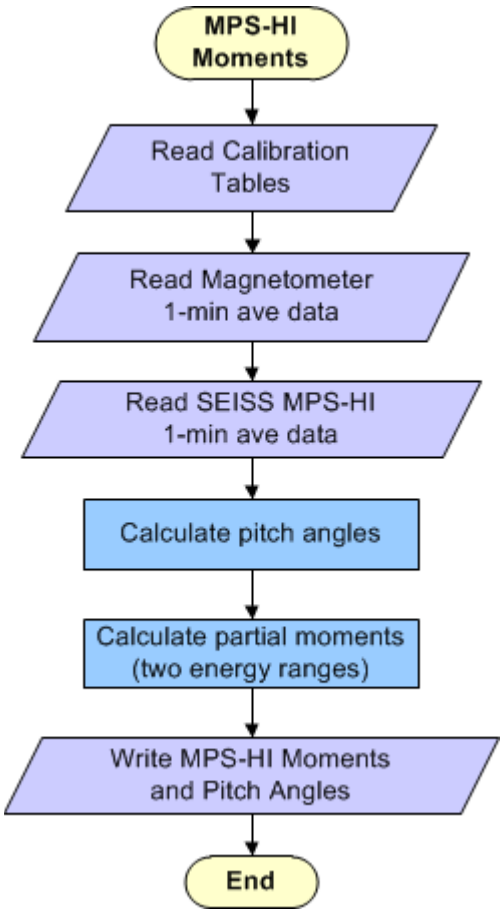

Figure 1. Top-level flow diagram for the MPS-HI Moments algorithm.

The corresponding processing outline for MPS-HI moments is as follows:

1. Read MPS-HI calibration processing parameter file (HDF5 format) whose version number is a global attribute of the MPS-HI L1b files. Calculate channel edge and center momenta (for electrons) or velocities (for protons), and conversion factors from flux to phase space density (for electrons) or velocity distribution (for protons).

2. Read MPS-HI telescope calibration file (HDF5 format), which contains telescope angles and telescope-inclusion table. Calculate telescope direction cosines from angles.

3. Read in the 1-minute averages of the MAG field components in body reference frame (BRF) coordinates and associated time stamp.

4. Read in the 1-minute averages of the MPS-HI differential number fluxes and associated time stamp.

5. If time stamps of fluxes and field components are identical, proceed.

6. If magnetic field values are not missing (indicated by fill values), calculate the central pitch angle for each MPS-HI telescope from the MAG field components in body-reference-frame coordinates. If they are missing, no moments are calculated from this minute of data.

7. For pitch angles greater than 90 degrees, take the supplementary angle. Sort resultant pitch angles in ascending order. Calculate pitch angle integration limits.

8. If so indicated by MPS-HI telescope-inclusiontable, force omission of a given telescope by replacing fluxes with fill values.

9. For each energy channel and species (electron or proton), count the number of fill values. If this number is greater than one for any channel, do not calculate moments for that species.

10. If there is one fill value for a given energy channel, linearly interpolate versus pitch angle or (at edges) replace with nearest neighbor.

11. Calculate the partial moments (number density, parallel temperature and perpendicular temperature) in two energy ranges, for electrons and protons.

12. Record the Level 2 outputs and quality flags.

The top-level processing flow for the MPS-LO algorithm is shown in Figure 1. At this level there are two decision points, each of which results in the selection of one of two branches. The corresponding processing outline is as follows:

1. Read MPS-LO calibration processing parameter file whose version number is a global attribute of the MPS-LO L1b files. Calculate channel edge and center velocities and conversion factors from flux to velocity distribution.

2. Read MPS-LO zonal calibration file (HDF5 format), which contains zonal angles, zone-inclusion table, and weights for combining overlapping zones Z6 and Z7. Calculate zonal direction cosines from angles.

3. Read in the 1-minute averages of the MAG field components in body frame coordinates and associated time stamp.

4. Read in the 1-minute averages of the MPS-LO differential number fluxes and eclipse flags and associated time stamp.

5. If time stamps of fluxes, field components and spacecraft flags are identical, proceed.

6. If magnetic field values are not missing (indicated by fill values), calculate the central pitch angle for each MPS-LO zone from the MAG field components in body-frame coordinates. If they are missing, no moments are calculated from this minute of data.

7. Sort pitch angles in ascending order. Calculate pitch angle integration limits.

8. If so indicated by zone-inclusion table, force omission of a given zone by replacing fluxes with fill values.

9. For each energy channel and species (electron or proton), count the number of fill values. If more than one for any channel, do not calculate moments for that species.

10. If there is one fill value for a given energy channel, linearly interpolate versus pitch angle or (at edges) replace with nearest neighbor.

11. Calculate an initial omnidirectional average of the electron and ion differential energy fluxes.

12. In the omnidirectional electron energy fluxes, search for the signature of trapped secondary electrons or photoelectrons. If this signature is present, identify the barrier potential and set the omnidirectional and differential electron fluxes below the corresponding energy to zero.

13. In the omnidirectional ion energy fluxes, search for the signature of surface charging known as the 'ion line.' If the 'ion line' can be identified clearly, estimate the spacecraft potential from this signature.

14. If the 'ion line' cannot be identified clearly, estimate the spacecraft potential from the omnidirectional electron temperature. This is an iterative solution that uses a correlative relation between the electron temperature and spacecraft potential. (*Turned off at launch until correlative relation has been established.*)

15. Use the estimated spacecraft potential to correct the electron and ion energy scale.

16. Calculate the partial moments (number density, parallel temperature and perpendicular temperature) for electrons and protons in the MPS-LO energy range.

17. Record the Level 2 outputs and quality flags.

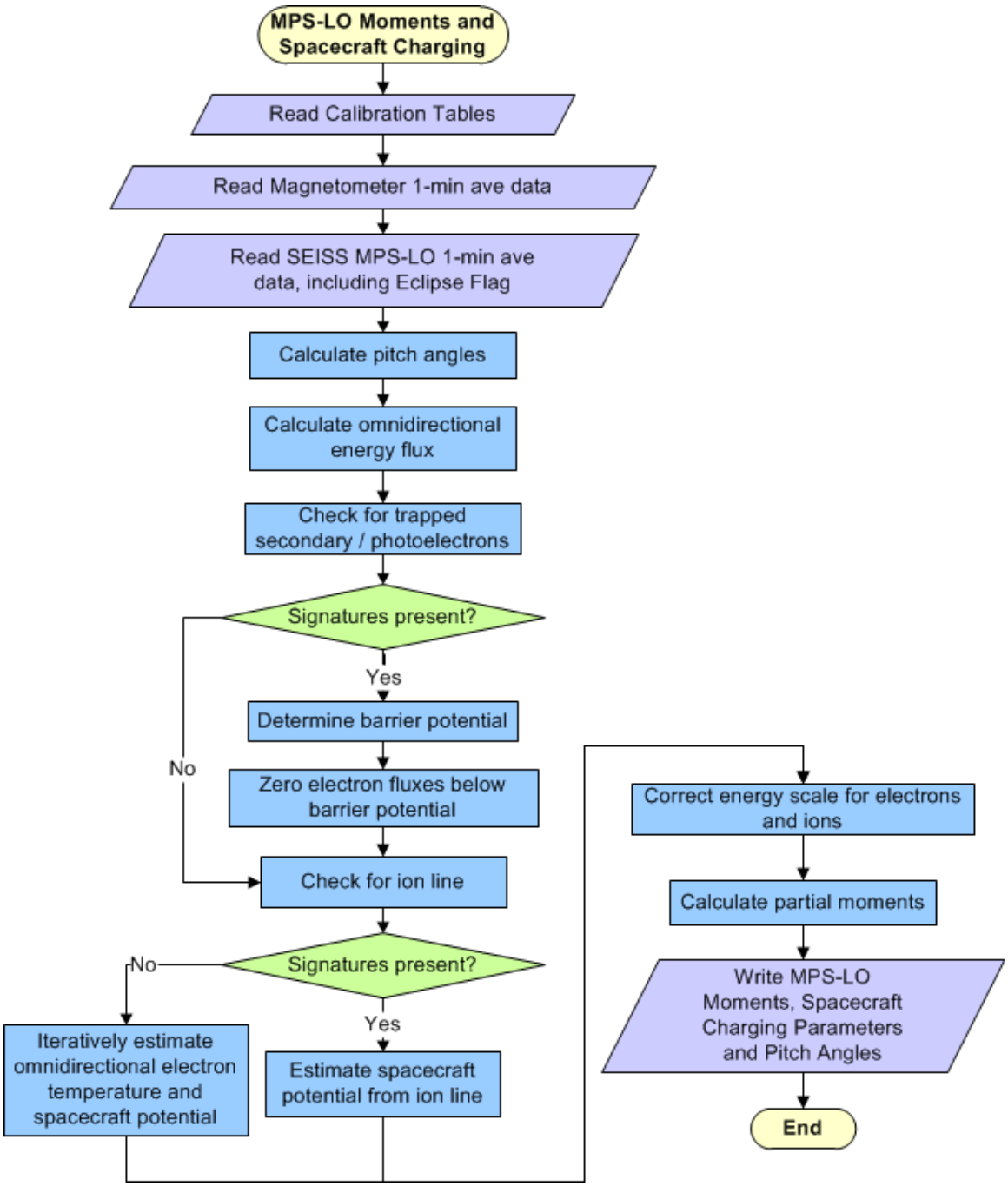

Figure 2. Top-level flow diagram for the MPS-LO Moments and Level of Spacecraft Charging algorithm.

3.3 Algorithm Input

Input quantities are single-precision floating point except for Julian date (double precision floating point) and version numbers (integers).

3.3.1 Sensor Data

The inputs to the Moments algorithms from MPS-LO, MPS-HI and MAG are listed in separate tables (Table 1, Table 2, Table 3).

The spacecraft eclipse flag indicates when the spacecraft is eclipsed from the Sun by the earth. It is needed for the MPS-LO Moments algorithm since the correlative relationship between frame potential and electron temperature depends on whether the spacecraft is in eclipse.

Table 1. MPS-LO inputs to moments and spacecraft charging algorithm.

Quantity	**Sampling**	**Number of Values**	**Units**	**Purpose in L2 Calculations**
MPS-LO Electron Fluxes	1 min ave	15 channels x 14 zones	electrons / (cm^2 s sr keV)	<30 keV electron moments
MPS-LO Ion Fluxes	1 min ave	15 channels x 14 zones	ions / (cm^2 s sr keV)	<30 keV ion (proton) moments
Spacecraft eclipse flag	1 min OR	1	0: false, 1: true	Spacecraft charging level
Version of MPS-LO Calibration Processing Parameter File	1 min	1	unitless	To access the most up-to-date tables used to process the L1b fluxes
Version of MPS-LO Zonal Calibration File	1 min	1	unitless	To access most up-to-date table.
Time	1 min	1 (start of period)	Seconds since J2000 epoch	Time stamp

Table 2. MPS-HI inputs to moments algorithm.

Quantity	Sampling	Number of Values	Units	Purpose in L2 Calculations
MPS-HI Electron Fluxes	1 min ave	10 channels x 5 telescopes	electrons / (cm^2 s sr keV)	>30 keV electron moments
MPS-HI Proton Fluxes	1 min ave	9 channels x 5 telescopes	protons / (cm^2 s sr keV)	>30 keV proton moments
Version of MPS-HI Calibration Processing Parameter File	1 min	1	unitless	To access the most up-to-date tables used to process the L1b fluxes
Version of MPS-HI Telescope Calibration File	1 min	1	unitless	To access most up-to-date table.
Time	1 min	1 (start of period)	Seconds since J2000 epoch	Time stamp

Table 3. MAG inputs to moments and spacecraft charging algorithms.

Quantity	Sampling	Number of Values	Units	Purpose in L2 Calculations
Magnetometer Field Components in Body Reference Frame Coordinates	1 min ave	4 (3 components and total)	nT	Pitch angle calculation
Time	1 min	1 (start of period)	Seconds since J2000 epoch	Time stamp

3.3.2 Sensor Characterization Data

Several quantities that characterize the spectral and spatial response of the MPS-LO and MPS-HI are used by the Moments algorithms. These quantities are listed in Table 4.

Table 4. Sensor characterization data used by Moments algorithms. All of these data reside in files with standardized names that are distinguished by version number.

Quantity	Refresh	Number of Values	Units	Purpose	Source
MPS-LO Zone Center Direction in Spacecraft Coordinates	Static	14 zones x 2 angles (azimuth and elevation)	degrees	Pitch angle calculation	MPS-LO Zonal Calibration File
MPS-LO Channel Center Energies	Static, subject to revision	Electrons: 14 x 15 Ions: 14 x 15	keV	Integration grid points for moments calculations	MPS-LO Calibration Processing Parameter File
MPS-HI Telescope Center Direction in Spacecraft Coordinates	Static	5 telescopes x 2 angles (azimuth and elevation)	Azimuth and elevation (degrees)	Pitch angle calculation	MPS-HI Telescope Calibration File
MPS-HI Channel Edge Energies	Static, subject to revision	Electrons: 5 x 10 x 2 Protons: 5 x 9 x 2	keV	Integration grid points for moments calculations	MPS-HI Calibration Processing Parameter File

3.4 Theoretical Description

In order to focus on the algorithm in this section, background information and extended derivations are provided in the appendices.

3.4.1 Physics of the Problem

Moments

In general, magnetospheric electron and proton fluxes are a function of particle kinetic energy and of look direction. Particle flux measurements are commonly converted to doubly differential fluxes (fluxes that are differential in energy and in solid angle) via calibration factors. The angular variation of the fluxes is expressed in spherical coordinates. The polar angle is identified with the particle pitch angle, that is, the angle that the particle's velocity makes with the magnetic field. Because of the relatively few angular measurements by the GOES instruments, we must assume that the fluxes are isotropic in azimuth angle around the magnetic field (i.e., gyrotropic). Therefore, all angular variation is attributed to pitch angle. The assumption of gyrotropy is not necessary with instruments on spin-stabilized spacecraft (such as ISEE or the LANL instruments in geostationary orbit) multiple samples during the spin cycle provide an additional dimension of angular sampling not available to instruments on a three-axis stabilized satellite.

For many applications, both scientific and operational, there is a need to reduce the fluxes to a handful of parameters. It is common practice to convert flux measurements to number density, velocities (not always possible), and energy density or the related quantities pressure and temperature [*DeForest and McIlwain*, 1971; *Daglis et al.*, 1994; *Thomsen et al.*, 1996, 1999]. Mathematically, these quantities can be expressed as moments of the distribution of particles in configuration (x, y, z) space and velocity (v_x, v_y, v_z) space, often referred to as the velocity distribution. The number density is the zeroth-order moment, the velocity is the first-order moment, and the energy density or temperature is derived from the second-order moment of the velocity distribution. For relativistic particles (in the present application, MPS-HI electrons), the moments need to be calculated using the phase space density (the distribution of particles in relativistic momentum and configuration space).

Number density is a differential quantity and can vary as a function of pitch angle (since populations at different pitch angles may originate in different locations in the magnetosphere). Therefore, the number density reported by the moments algorithm is the average of number densities in all directions. Under the assumption of gyrotropy, two temperatures can be calculated, namely the temperature of the distribution parallel to the

magnetic field and the temperature perpendicular to the magnetic field. The velocity moments are difficult to calculate from particle measurements in general and are not possible from those on GOES-R. It is possible if the drift velocity of the distribution is much greater than the mean thermal velocity of the distribution. From the LANL satellites, only the velocities for the <100 eV ions are generally physically meaningful and are reported to the general community [M. Thomsen, private communication, 2009]. The assumption of gyrotropy means that only an along-field velocity could be calculated. However, attempts to calculate this component (which would be of limited value in any case) from the proxy data under conditions where the drift velocity is significant (i.e., the magnetosheath [*McComas et al.*, 1994]) have not been successful. (See section 6 for more details.)

The energy density of a distribution is meaningful regardless of the distribution, but the related quantity temperature strictly speaking applies to a Maxwellian distribution, which is in equilibrium. Particle distributions in the magnetosphere are sometimes but not generally well modeled as a Maxwellian. However, due to a long history of calculating the temperature of a distribution [e.g., *Garrett et al.*, 1980; *Gussenhoven and Mullen*, 1983; *Thomsen et al.*, 1999] and since the temperature of a distribution is a critical parameter in spacecraft charging codes (NASCAP-2k), we stick with this nomenclature. If the measured distribution is a Maxwellian, the 'temperature' moments give the temperature (in fact, kT in units of keV). If the measured distribution is not Maxwellian, the temperature moment is still a useful measure of the spectral variation in the fluxes. A higher temperature gives higher fluxes at higher energies relative to a lower temperature distribution of similar number density.

For the more general relativistic case, the momentum phase space density is used in place of the velocity distribution. The phase space density is the number density of particles per unit relativistic momentum in three directions. While the number density integral is similar to the non-relativistic case, the temperature integral is more complicated. In fact, the average energy of a relativistic Maxwellian is not proportional to the temperature, but rather is a transcendental function of the temperature [*Jüttner*, 1911; *de Groot et al.*, 1980]. For this moments algorithm, the non-relativistic moments are calculated for all protons/ions and for MPS-LO electrons (<= 30 keV). Relativistic moments are calculated for MPS-HI electrons (>50 keV).

Since the energy ranges of the instruments are limited, it is strictly correct to refer to the densities and temperatures that we calculate as 'partial.' For maximum user flexibility, we calculate densities and temperatures for three energy ranges and do not combine them. In principle, the combination is straightforward (see section 6), though performed with greater confidence after the instruments have been intercalibrated.

Spacecraft Charging

Geosynchronous spacecraft tend to charge to a large negative potential in the absence of a dense, cold plasmasphere [*DeForest*, 1972]. For example, on the ATS-6 satellite, negative potentials as large as 19 kV in eclipse and 2 kV in sunlight were observed [*Olsen*, 1986]. The potentials observed on ATS-6, which was three-axis stabilized, were larger than those observed on ATS-5, which was spin-stabilized [*Olsen*, 1986]. Charging occurs as the system attempts to balance currents due to incident electrons and positive ions, secondary electrons emitted by the spacecraft due to the incident particle environment, and photoelectrons emitted by the spacecraft due to incident ultraviolet sunlight [*Garrett*, 1981]. This phenomenon is referred to as surface charging or, more accurately depending on the observation, as frame charging. The surface potential, which is the potential between a spacecraft surface and the spacecraft frame (electrical ground), is distinct from the frame potential, i.e., the potential between the spacecraft frame and the surrounding plasma, which is what plasma sensors such as MPS-LO measure [*Koons et al.*, 2006]. The incident electrons that contribute to surface charging have energies less than ~100 keV. The danger of spacecraft charging lies not in the charging itself but in the discharges that occur when the differential potential becomes sufficiently large. This can happen with frame charging when the spacecraft exits eclipse. Differential surface charging has been identified as the likely cause of some spacecraft anomalies and failures on orbit [e.g., *Farthing et al.*, 1982].

At higher energies, the electrons can penetrate materials, and the phenomenon is known as bulk or deep dielectric charging. For example, >450 keV electrons can penetrate 5 mils of aluminum, which is equivalent to 10 mils of spacecraft multi-layer insulation [*Fennell et al.*, 2010]. Deep dielectric charging has also been identified as the likely cause of some spacecraft anomalies and failures on orbit [e.g., *Baker*, 1996].

The GOES-R+ MPS measurements will contribute to the diagnosis of both frame and bulk charging on the GOES-R+ satellite and to the real-time specification of geosynchronous environments that present an elevated risk of spacecraft in general. However, only the MPS-LO measurements are affected by charging, specifically frame charging. At the same time that they can be used to diagnose frame charging on the spacecraft, they must be corrected for the effects of frame charging on the measured electron and ion spectra.

Uniform frame charging can be diagnosed by a peak in the ion spectrum (known as the ‘ion peak’ or ‘ion line’) at the spacecraft potential [*DeForest*, 1972; *Thomsen et al.*, 1999]. Differential frame charging results in the trapping of secondary electrons and photoelectrons behind a barrier potential [*Whipple*, 1976]. This barrier potential can be diagnosed from the electron spectrum [*Thomsen et al.*, 1999]. Examples of both phenomena can be observed in a sample pair of electron and ion spectrograms from the Los Alamos National Laboratory (LANL) Magnetospheric Plasma Analyzer (MPA) instrument flown on geosynchronous spacecraft [*Bame et al.*, 1993; *McComas et al.*,

1993] (Figure 3). Shortly after 1700 UT on 2 November 2003, the electron fluxes below ~10 eV increased an order of a magnitude and a weak peak appeared in the ion fluxes at ~60 eV. The upper limit of the electron flux enhancement and the energy of the ion line increased with time. The maximum in both was reached shortly after 1900 UT. The spectra from 1950 UT are shown in Figure 4.

The enhancement in the electron flux represented the trapped secondary electrons and photoelectrons. The ion line indicated the time-varying spacecraft frame potential; all measured ions had their energy increased by this amount. Both the barrier potential and the spacecraft potential were identified by the algorithm (indicated as blue traces on the spectrogram). The spacecraft potential from the ion line is plotted on both the electron and the ion spectra. At the peak of the charging event, the frame potential was an order of magnitude higher than the local potential barrier in the vicinity of the instrument.

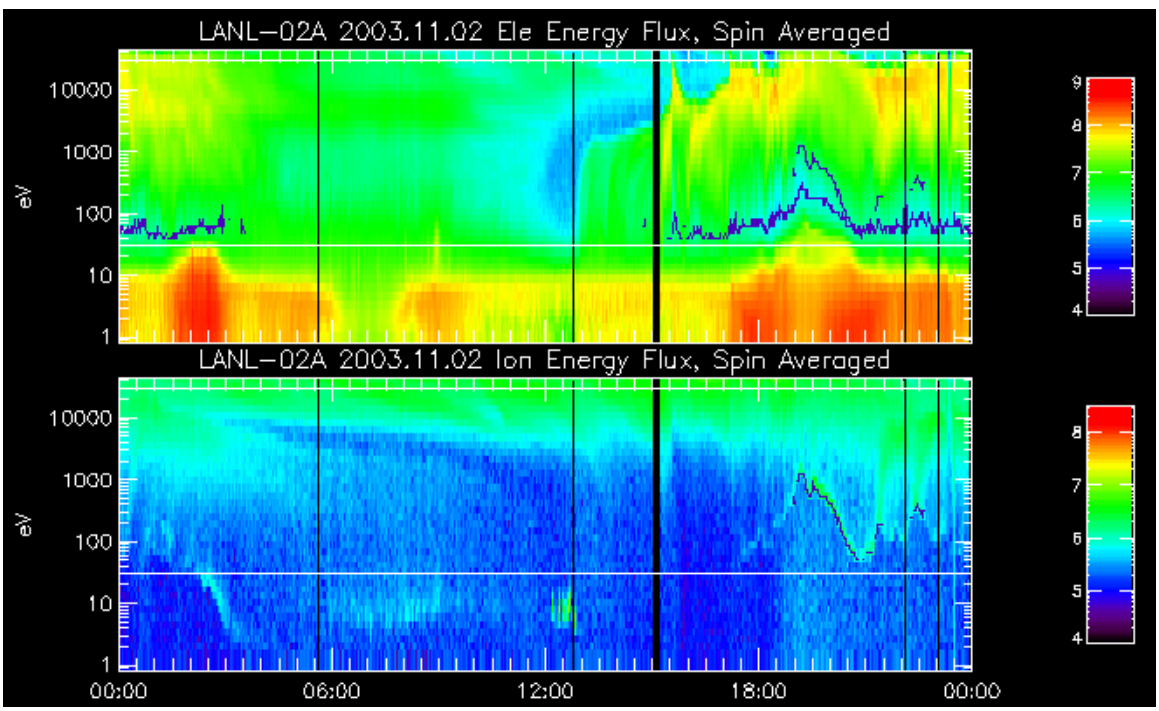

Figure 3. Spectrograms of spin-averaged electron and ion energy differential fluxes measured by the LANL MPA instrument on 2 November 2003. The horizontal axis represents universal time. The vertical axis represents the energies of the particles in electron volts (eV). The color scale represents the base-10 logarithm of the energy flux in units of eV cm^{-2} s^{-1} sr^{-1} eV^{-1}. Examples of trapped secondary and photoelectrons and the ion line can be observed in the fluxes after 1700 UT. The dark blue traces represent the identification by the algorithm of the frame potential and barrier potential. MPA data provided courtesy of M. Thomsen, Los Alamos National Laboratory.

In order to better represent the unperturbed flux outside the spacecraft sheath, the measured ion energy should be reduced by the frame potential and the measured electron energy should be increased by this amount. Because of the finite width of the energy channels (coarser on MPS-LO than on MPA), this process introduces errors that should be flowed through the moments calculation. Electrons below the barrier potential should not be included in a representation of the unperturbed flux [*Whipple*, 1976] or in the moments calculation [*Thomsen et al.*, 1999]. This would artificially increase the derived number density and decrease the temperatures.

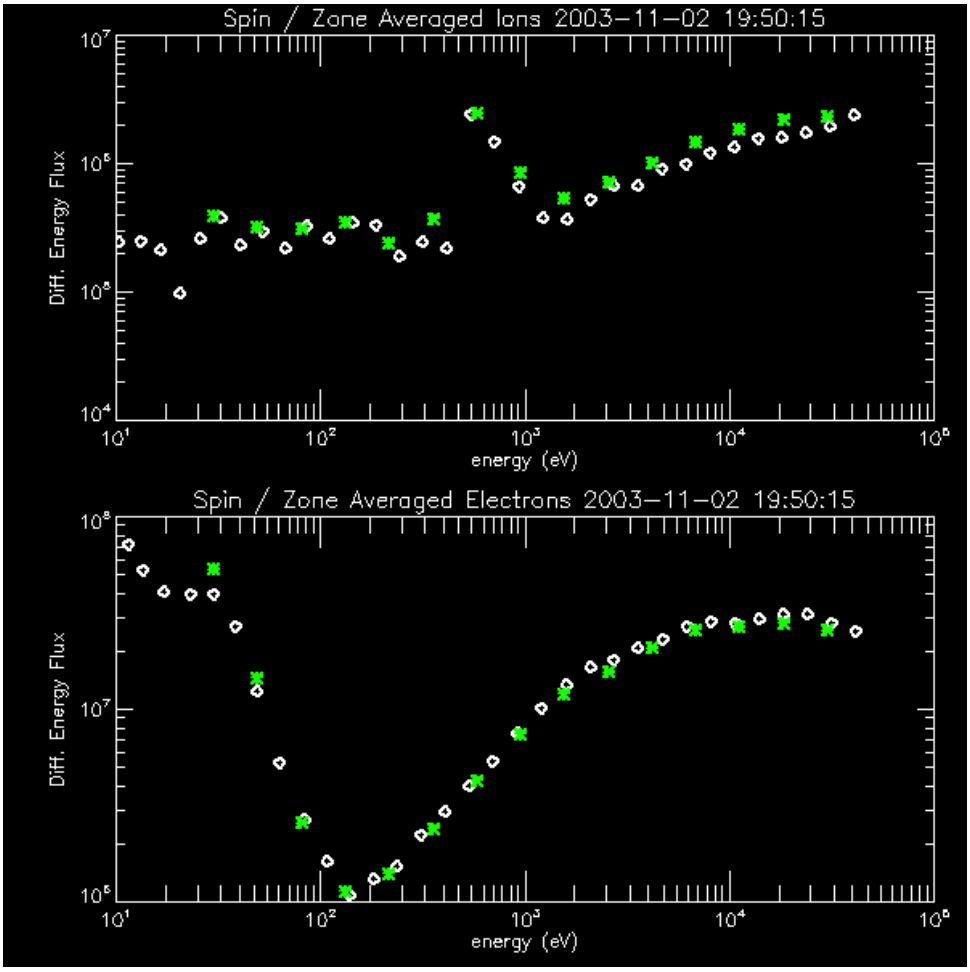

Figure 4. An example of spin-averaged ion and electron spectra from the LANL-02A MPA on 2 November 2003, 1950:15 UT. Based on these data, the barrier potential is estimated to be -150 eV and the spacecraft frame potential is estimated to be -700 V. MPA data provided courtesy of M. Thomsen, Los Alamos National Laboratory.

The temperature of the incident electron spectrum has been correlated with the frame potential of the spacecraft [e.g., *Garrett et al.*, 1980; *Thomsen et al.*, 1999]. This

correlation depends on the spacecraft and whether the spacecraft is in eclipse. An example from the LANL satellites is shown in Figure 5. Such a correlation can be used for estimating the spacecraft frame potential in the absence of a detectable ion line, which can happen when the cold ion population is particularly tenuous [*Gussenhoven and Mullen*, 1983].

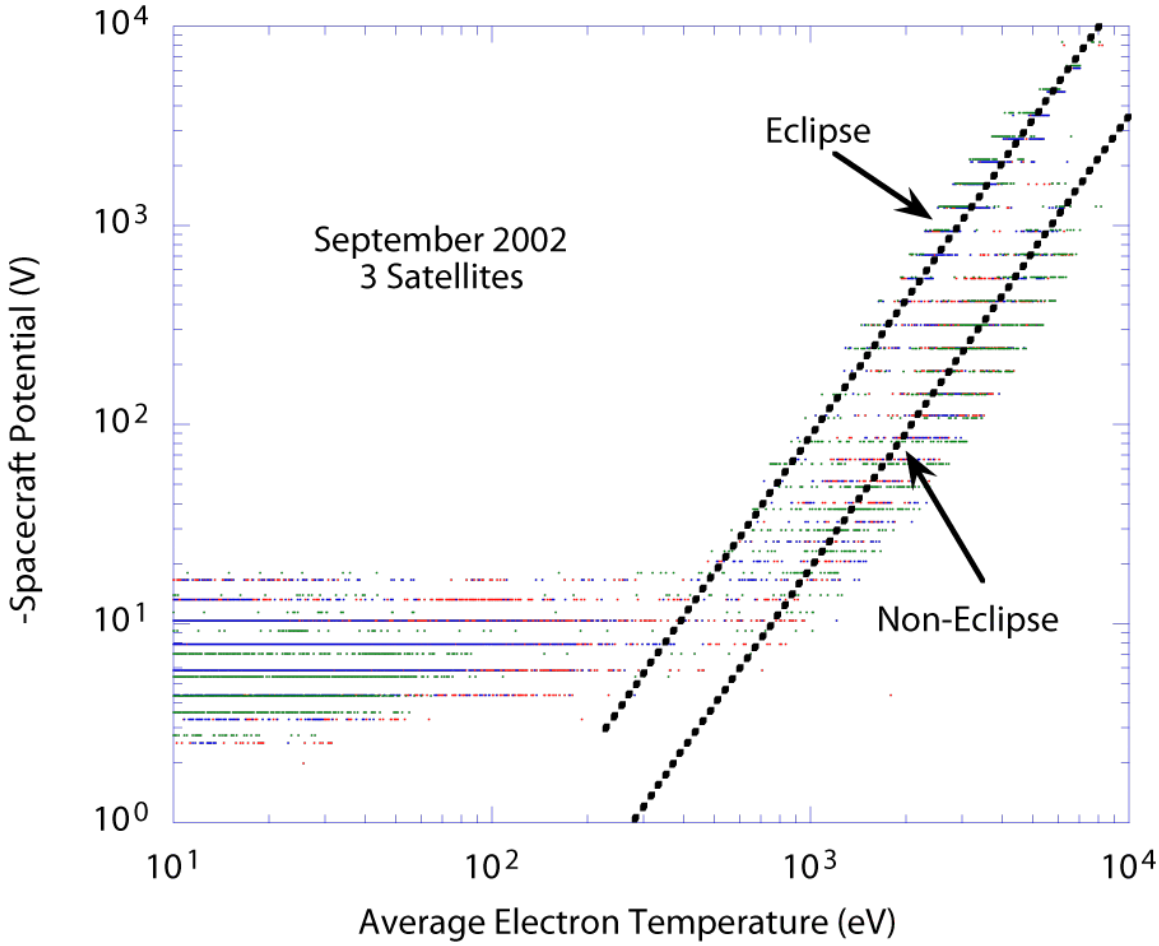

Figure 5. Spacecraft potential vs. average electron temperature from three geosynchronous satellites (1994-084, LANL-97A, LANL-02A) in September 2002. Separate fits to eclipse and non-eclipse conditions are shown. Figure courtesy of M. Thomsen, Los Alamos National Laboratory.

3.4.2 Mathematical Description

Calculation of Pitch Angle

The calculation of the central pitch angle for each MPS telescope or zone requires knowledge of the look angles of the telescope or zone with respect to the spacecraft body reference frame (BRF) coordinate axes, and the values of the magnetic field components in the BRF as measured by the GOES-R Magnetometer. Remember that the pitch angle

is the angle that the particle velocity makes with respect to the magnetic field, and therefore is oppositely directed to the telescope look direction. It is is the polar angle in a spherical coordinate system where the pole is defined by the local direction of the magnetic field. Therefore, the direction cosines used in the calculation of pitch angle are those of the velocities of the particles measured by the telescope or zone. Given l_x, l_y, and l_z as the BRF direction cosines of the particle velocities measured by telescope or zone k, the central pitch angle for telescope k is given by

$$\alpha_k = \arccos\left(\frac{B_x l_x + B_y l_y + B_z l_z}{B_t}\right) \tag{1}$$

Note that within the accuracy of the magnetic field measurements, it is possible that, in the case of zero pitch angle (a rare event, especially in a one-minute average), the argument of the inverse cosine could be slightly greater than one. This condition should be checked prior to calculating the pitch angle.

For MPS-HI (and MAGED and MAGPD), since there are few angular measurements in the north-south or meridional plane, we have to assume that the pitch angle distribution between 90 and 180 degrees is the same as the distribution between 90 and 0 degrees. Therefore, any pitch angle greater than 90 degrees is replaced by its supplementary angle (180°-α). (This is not necessary for MPS-LO.) Then, the pitch angles are sorted in ascending order and the sorted indices also saved for use in sorting the electron and proton fluxes.

If one or more of the magnetic field components is a fill value, then the pitch angles cannot be calculated, and the moments calculation is skipped. Note that the magnetic field values, flux values, and spacecraft flags used in a given moments calculation must all have the same time stamp. They are all assumed to be outputs of the L2 1-minute averages algorithm.

Treating the Fluxes

From MPS-LO, the two overlapping zones 6 and the two overlapping zones 7 are respectively combined using the weights contained in the zonal calibration table. For now, these weights are assumed to be 0.5. They are expected to change following on-orbit cal/val and will probably be different for electrons and ions.

The fluxes are sorted by ascending pitch angle.

If a flux fill value is present and there is at most one fill value in each energy channel (i.e., the PAD at each energy is missing at most one flux value), then the fill value is replaced by its nearest neighbor (if at the lowest or highest pitch angle) or by the linear

interpolation (in pitch angle space) of its two neighbors, after the fluxes have been sorted by ascending pitch angle.

Determination of the Level of Spacecraft Frame Charging

The level of spacecraft surface or frame charging is determined from an omnidirectional average of the MPS-LO fluxes. Each of the twelve zones is weighted properly by a factor related to its central pitch angle. The omnidirectional flux is expressed as the following integral:

$$j_{omni}(E_i) = \frac{\int_0^{\pi} j(\alpha, E_i)\sin\alpha\, d\alpha}{\int_0^{\pi} \sin\alpha\, d\alpha} = \frac{1}{2}\int_0^{\pi} j(\alpha, E_i)\sin\alpha\, d\alpha \tag{2}$$

This integral is approximated as the following sum:

$$j_{omni}(E_i) = \frac{1}{2}\sum_{j=0}^{N_{pa}-1} j(\alpha_j, E_i)\left(-\cos\alpha_{j,u} + \cos\alpha_{j,l}\right) \tag{3}$$

The omnidirectional flux is converted to a velocity distribution for later use:

$$f_{v,omni}(v_i) = \frac{m_o}{v_i^2}\, j_{omni}(E_i) \tag{4}$$

Next, the number fluxes are converted to energy flux simply by multiplying the number flux by the channel energy (energy to which the electrostatic analyzer steps):

$$j_{E,omni}(E_i) = E_i\, j_{omni}(E_i) \tag{5}$$

The following algorithm, closely based on that of *Thomsen et al.* [1999], is used to identify and remove trapped secondary electrons or photoelectrons:

1. Search for the minimum in the omnidirectional average of the electron differential energy flux below 400 eV.
2. If the minimum is above 100 eV, identify it as the barrier potential only if the average electron differential energy flux above 3 keV is greater than 2.4 x 10^6 cm^{-2} s^{-1} sr^{-1} (eV/eV) (TBR)
3. Set all electron flux below the barrier potential equal to zero, record the barrier potential, and set the associated data quality flag.

If this source of contamination is not removed, the number density will be too high and the temperature will be too low.

The next step is to identify the ion line. Again, the algorithm is closely based on that of *Thomsen et al.* [1999]:

1. If the average ion differential energy flux above 3 keV is less than 0.8 x 10^7 (spacecraft eclipse) or 1.3 x 10^7 (sunlit) cm^{-2} s^{-1} sr^{-1} (eV/eV) (TBR), search for a peak in the ion flux below 150 eV.
2. If the average ion differential energy flux above 3 keV is greater than the above criteria, search below 9 keV.
3. Starting at the lowest ion energy (30 eV), search for a 2x increase in the ion fluxes from one energy channel to the next.
4. If this ion flux is a local maximum (in energy), identify the channel energy at peak as $-q\varphi_{sc}$
5. If the ion energy flux at the next higher energy is higher, followed by a drop, identify the channel energy at the peak as $-q\varphi_{sc}$
6. The ion flux at the peak must be at least twice the single count level
7. Set the ion line quality flag and record φ_{sc}

If no ion line can be identified, the spacecraft potential is estimated from an empirical relation between electron temperature and spacecraft potential. The following three expressions are solved iteratively for the omnidirectional average of the electron density, the electron temperature and the spacecraft potential:

$$n_{omni} = 4\pi \int f_{v,omni}(v) v^2 dv = \frac{4\pi}{3} \sum_{i=0}^{N_{ch}-1} f_{v,omni}(v_i)\left(v_{i,u}^3 - v_{i,l}^3\right) \tag{6}$$

$$T_{omni} = \frac{4\pi m}{3n_{omni}} \int f_{v,omni}(v) v^4 dv = \frac{4\pi m}{15n} \sum_{i=0}^{N_{ch}-1} f_{v,omni}(v_i)\left(v_{i,u}^5 - v_{i,l}^5\right) \tag{7}$$

$$-\Phi_{sc} = A + B\left(\frac{T_{e,omni}}{T_o}\right)^D \tag{8}$$

The last expression is an empirical relation for spacecraft potential vs. electron temperature developed for the LANL geosynchronous measurements [*Thomsen et al.*, 1999]. An example of this relation and the data from which it was determined are shown in Figure 5. Values for these constants are given in Table 5. These values will definitely need to be freshly evaluated for each GOES-R+ satellite after launch. It is possible that a different empirical function will also need to be developed.

Table 5. Values of the constants used in the empirical relation between electron temperature and spacecraft potential. These values will need to be reevaluated for each GOES-R+ satellite.

Constant	Value	Source
A	7.9	*Thomsen et al.*, 1999, Table 6
B (average)	0.015025	*Thomsen et al.*, 1999, Table 6
B (sunlit)	0.0069	Figure 5
B (spacecraft eclipse)	0.047	Figure 5
T_o	46.074 eV	*Thomsen et al.*, 1999, Table 6
D	2.4257	*Thomsen et al.*, 1999, Table 6

After the spacecraft potential has been determined from the empirical relation or from the ion line, the channel energies are corrected prior to calculating the moments to give the energies at infinity of the measured particle fluxes:

$$E_{corr} = E_{meas} + q\Phi_{sc} \tag{9}$$

Note that φ_{sc} and q are signed quantities. We expect that φ_{sc} will be negative. For a negative potential, the corrected ion energies are less than the measured energies, and the corrected electron energies are greater than the measured energies.

The 9 keV criterion for the maximum energy at which the ion line is detected directly was set by LANL to avoid false positives from the "deep ion minimum" [M. Thomsen, private communication, 2010]. The deep ion minimum corresponds to trajectories of ions injected on the nightside whose drift and bounce motions cause them to be lost via collisions with atmospheric particles [*McIlwain*, 1972; *McIlwain and Whipple*, 1986]. This common feature in geosynchronous orbit is a minimum in fluxes whose energy varies from ~10 keV at 0200 local time to ~1 keV at 1800 local time [*McIlwain*, 1972]. The expression that expresses spacecraft potential in terms of the electron temperature should account for any potentials above 9 keV, if the dataset from which the empirical expression is derived includes such cases.

The TBRs are associated with parameters that have been converted from the original criteria of *Thomsen et al.* [1999] in terms of counts measured by the LANL instruments, to flux-based criteria that should work with a different instrument. The conversion is not exact due to different instrument response functions and energy range, so these parameters will need to be validated post-launch.

Non-Relativistic Moment Integrals

The partial moments are calculated non-relativistically for the MPS-LO electrons and ions and for the MPS-HI protons. The benefits include relative simplicity with respect to

the relativistic formulation, and consistency with the LANL moments algorithm [*Thomsen et al.*, 1996, 1999].

Once the flux is determined as a function of kinetic energy and pitch angle, the non-relativistic velocity distribution is calculated ($s^3\ cm^{-6}$):

$$f_v(\alpha_{k,} v_i) = \frac{m_o}{v_i^2}\, j(\alpha_{k,} E_i) \tag{10}$$

The zeroth order moment of the velocity distribution in spherical coordinates, assuming no variation in azimuth (gyrotropy), is given by (cm^{-3}):

$$n = 2\pi \iint f_v(\alpha, v) v^2 \sin(\alpha) d\alpha\, dv \tag{11}$$

It is implemented as a sum following the LANL method [*Thomsen et al.*, 1996, 1999]. In this approach, the velocity distribution is assumed to be uniform over the energy-pitch angle bin.

$$n = \frac{2\pi}{3} \sum_{j=0}^{N_{pa}-1} \sum_{i=0}^{N_{ch}-1} f_v(\alpha_j, v_i)(-\cos\alpha_{j,u} + \cos\alpha_{j,l})(v_{i,u}^3 - v_{i,l}^3) \tag{12}$$

The second-order velocity moments giving parallel and perpendicular temperature (in keV) are given by:

$$T_{para} = \frac{2\pi m}{n} \int f_v(\alpha, v) v^4 \cos^2(\alpha) \sin(\alpha) d\alpha\, dv \tag{13}$$

$$T_{perp} = \frac{\pi m}{n} \int f_v(\alpha, v) v^4 \sin^3(\alpha) d\alpha\, dv \tag{14}$$

(See Appendix B for the evaluation of these integrals for non-relativistic Maxwellians.) As justified earlier, we assume that the first-order velocity moment is zero.

These integrals are approximated as sums using the same method as the density integral:

$$T_{para} = \frac{2\pi m}{15n} \sum_{j=0}^{N_{pa}-1} \sum_{i=0}^{N_{ch}-1} f_v(\alpha_j, v_i)(-\cos^3\alpha_{j,u} + \cos^3\alpha_{j,l})(v_{i,u}^5 - v_{i,l}^5) \tag{15}$$

$$T_{perp} = \frac{\pi m}{5n} \sum_{j=0}^{N_{pa}-1} \sum_{i=0}^{N_{ch}-1} f_v(\alpha_j, v_i)\left[\frac{3}{4}(-\cos\alpha_{j,u} + \cos\alpha_{j,l}) + \frac{1}{12}(\cos 3\alpha_{j,u} - \cos 3\alpha_{j,l})\right](v_{i,u}^5 - v_{i,l}^5) \tag{16}$$

Relativistic Moment Integrals

The partial moments are calculated relativistically for the MPS-HI electrons. Under the special theory of relativity, kinetic energy is not simply proportional to the square of velocity (see Appendix A), so the second moment of the relativistic velocity distribution cannot be used to calculate temperature. The general practice in radiation belt studies involving relativistic electrons is to use the phase space density [e.g., *Roederer*, 1970; *Onsager et al.*, 2004], which is relativistically correct. Phase space density, F_p (keV^{-3} s^{-3}), is calculated by dividing the differential flux by the square of the momentum of the particle, p (keV s cm^{-1}):

$$F_p = \frac{j}{p^2} \tag{17}$$

$$p = \frac{1}{c}\sqrt{E\left(E + 2m_o c^2\right)} \tag{18}$$

where E is the kinetic energy of the particle, m_o is the rest mass, and c is the speed of light (cm s^{-1}). Note that $m_o c^2$ is the rest mass of the particle in energy units (keV) and is used as such throughout this algorithm in order to simplify the calculations and unit conversions. Since the MPS-HI effective channel energies do not change due to spacecraft charging, the energies are converted to momentum at the start of run-time.

The relativistic number density integral (cm^{-3}) is defined over momentum space but otherwise is analogous to the the non-relativistic version:

$$n = 2\pi \iint F_p(\alpha, p) p^2 \sin(\alpha) d\alpha\, dp \tag{19}$$

It is implemented as a sum as follows (assuming the phase space density is uniform over the momentum-pitch angle bin):

$$n = \frac{2\pi}{3} \sum_{j=0}^{N_{pa}-1} \sum_{i=0}^{N_{ch}-1} F_p\left(\alpha_j, p_i\right)\left(-\cos\alpha_{j,u} + \cos\alpha_{j,l}\right)\left(p_{i,u}^3 - p_{i,l}^3\right) \tag{20}$$

The solution for the temperature moment is by no means as straightforward. The average energy of a relativistic Maxwellian is a transcendental function of the temperature [*Jüttner*, 1911; *de Groot et al.*, 1980], so after calculating the appropriate moment of the phase space density, there is another step to convert it to temperature. (See Appendix B for the analytical evaluation of the moments integrals for relativistic Maxwellians.)

We calculate the following moments (keV):

$$E_{T,para} = \frac{4\pi}{n} \iint EF_p(\alpha, p) p^2 \cos^2(\alpha) \sin(\alpha) d\alpha\, dp \tag{21}$$

$$E_{T,perp} = \frac{2\pi}{n} \iint EF_p(\alpha, p) p^2 \sin^3(\alpha) d\alpha\, dp \tag{22}$$

These two energies are related to the thermal energy of the distribution, excluding the rest mass (E is the kinetic energy). In the non-relativistic limit, these integrals give the perpendicular and parallel temperatures.

As a function of momentum and rest mass, kinetic energy is given by:

$$E = \sqrt{\left(m_o c^2\right)^2 + p^2 c^2} - m_o c^2 \tag{23}$$

Immediately, we can see that these integrals will be more complicated to solve than their non-relativistic equivalents. However, by assuming the phase space density is uniform over the momentum-pitch angle bin, an analytical approximation can be found (see Appendix C). Each term in the resulting sum includes a function of momentum h(p) ($keV^4\ s^3\ cm^{-3}$) given by:

$$h(p) = \frac{p}{4c^2}\left[\left(m_o c^2\right)^2 + p^2 c^2\right]^{\frac{3}{2}} - \frac{1}{8}\left(m_o c^2\right)^2 \frac{p}{c^2}\left[\left(m_o c^2\right)^2 + p^2 c^2\right]^{\frac{1}{2}}$$
$$- \frac{1}{8}\left(m_o c^2\right)^4 \frac{1}{c^3} \ln\left\{cp + \left[\left(m_o c^2\right)^2 + p^2 c^2\right]^{\frac{1}{2}}\right\} - \frac{1}{3} m_o c^2 p^3 \tag{24}$$

The energy integrals are approximated by:

$$E_{T,para} = \frac{4\pi}{3n} \sum_{j=0}^{N_{pa}-1} \sum_{i=0}^{N_{ch}-1} F_p\left(\alpha_j, p_i\right)\left(-\cos^3 \alpha_{j,u} + \cos^3 \alpha_{j,l}\right)\left[h\left(p_{i,u}\right) - h\left(p_{i,l}\right)\right] \tag{25}$$

$$E_{T,perp} = \frac{2\pi}{n} \sum_{j=0}^{N_{pa}-1} \sum_{i=0}^{N_{ch}-1} F_p\left(\alpha_j, p_i\right)\left[\frac{3}{4}\left(-\cos\alpha_{j,u} + \cos\alpha_{j,l}\right) + \frac{1}{12}\left(\cos 3\alpha_{j,u} - \cos 3\alpha_{j,l}\right)\right]\left[h\left(p_{i,u}\right) - h\left(p_{i,l}\right)\right] \tag{26}$$

For an isotropic, relativistic Maxwellian distribution, these integrals are equal to (see Appendix B):

$$E_T = \frac{2}{3} m_o c^2 g(\beta) = \frac{2}{3} m_o c^2 \left[\frac{K_1(\beta)}{K_2(\beta)} + \frac{3}{\beta} - 1\right] \tag{27}$$

where β is the rest mass (in energy units) divided by kT:

$$\beta = \frac{m_o c^2}{kT} \tag{28}$$

K_1 and K_2 are the modified Bessel functions of the second kind of orders 1 and 2. In the non-relativistic limit, $g(\beta) = 3/2\beta = 3kT/(2m_oc^2)$. It can be seen that E_T is greater than kT by comparing 3/2β with g(β) (Figure 6).

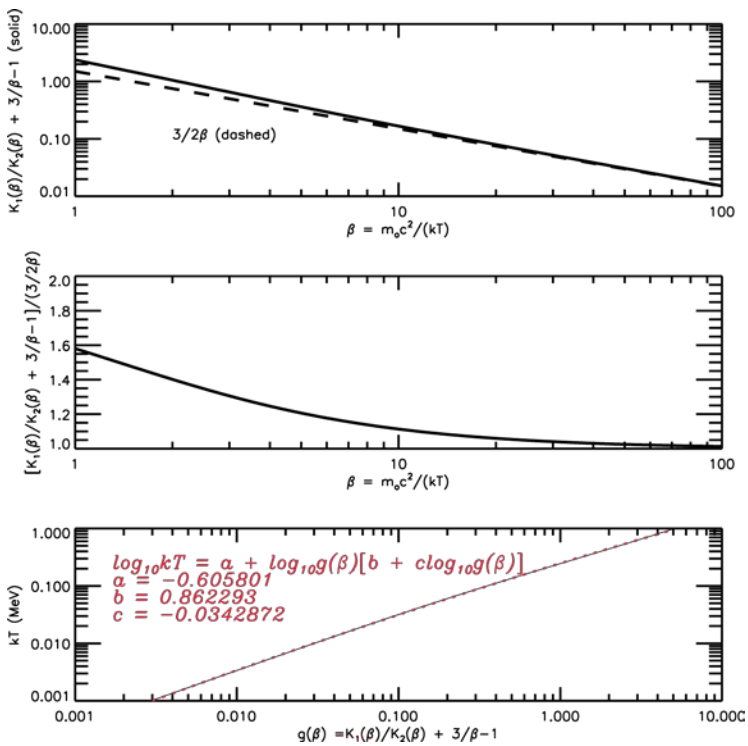

Figure 6. (Top) The function g(β) as a function of β. The non-relativistic equivalent is plotted with a dashed line. (Middle) The ratio of g(β) to its non-relativistic equivalent. (Bottom) Temperature kT as a function of g(β) (solid line), and the quadratic fit to this expression in log-log space (red dotted line).

If kT is expressed as a function of g(β) (Figure 6), this relation is nearly linear in log-log space. A quadratic fit gives:

$$\log_{10}(kT) = a + \log_{10}[g(\beta)]\{b + c\log_{10}[g(\beta)]\} \tag{29}$$

$$a = -0.605801$$
$$b = 0.862293$$
$$c = -0.0342872$$

By setting

$$g(\beta) = \frac{3}{2}\frac{E_T}{m_o c^2} \tag{30}$$

this fit can be used to convert the output of the integrals E_T to temperature kT without an iterative solution involving Bessel functions.

Definition of Integral Bin Limits

Following the LANL algorithm [*Thomsen et al.*, 1996, 1999], the velocity bin limits for the non-relativistic integrals correspond to the edges of the energy channels, $E_{i,l}$ and $E_{i,u}$:

$$v_{i,l} = \sqrt{\frac{2E_{i,l}}{m_o}} \tag{31}$$

$$v_{i,u} = \sqrt{\frac{2E_{i,u}}{m_o}} \tag{32}$$

For the relativistic integrals, the momentum bin limits also correspond to the edges of the energy channels:

$$p_{i,l} = \frac{1}{c}\sqrt{E_{i,l}\left(E_{i,l} + 2m_o c^2\right)} \tag{33}$$

$$p_{i,u} = \frac{1}{c}\sqrt{E_{i,u}\left(E_{i,u} + 2m_o c^2\right)} \tag{34}$$

The pitch angle bins are the same for the non-relativistic and relativistic integrals. They are the average of the central pitch angles, with the lowest limit set to 0 deg and the highest limit set to 90 deg for MPS-HI and to 180 deg for MPS-LO.

The MPS-HI channel edge energies and the MPS-LO channel center energies are documented in the Calibration Data Books (CDRL79) and are read in from the calibration processing parameter files whose version numbers are global attributes of the L1b files. The effective MPS-LO channel edge energies are calculated as geometric means of the center energies:

$$E_{i,u} = \sqrt{E_{i-1,c} E_{i,c}} \tag{35}$$

$$E_{i,l} = \sqrt{E_{i+1,c} E_{i,c}} \tag{36}$$

This follows the convention that the MPS-LO center energies decrease with increasing channel index. For the highest and lowest energies, the effective outer band edges are determined as follows. The MPS-LO center energies are nominally spaced equidistant in log(energy). The spacing is calculated as follows:

$$\Delta \log_{10}(E) = \frac{\log_{10}(E_1) - \log_{10}(E_n)}{n-1} \tag{37}$$

For MPS-LO, where n = 15, E_1 = 30 keV and E_{15} = 0.03 keV, this quantity is 0.2142857. Using the property of equidistant logarithmic spacing, it can be shown that the geometric-mean band edges above and below energy E_i are given by:

$$E_{i,u} = E_{i,c} \cdot 10^{+0.5\Delta \log_{10}(E)} \tag{38}$$

$$E_{i,l} = E_{i,c} \cdot 10^{-0.5\Delta \log_{10}(E)} \tag{39}$$

For $E_{1,c}$ = 30.0 keV, $E_{1,u}$ = 38.4 keV, and for $E_{15,c}$ = 0.030 keV, $E_{15,l}$ = 0.0234 keV. Although the actual energy centers differ from the nominal values, it is recommended that these upper and lower energies $E_{1,u}$ and $E_{15,l}$ be treated as fixed values since, in any case, the choice of band edges for an electrostatic analyzer with narrow ΔE/E is somewhat arbitrary.

Note that, for consistency with the LANL moments product, the lower limit of the MPS-LO moments integral is ~30 eV for the electrons and ~130 eV for the ions (in fact, the channels with corrected center energies closest to these values). These center energies vary with the amount of spacecraft charging, and the channel set included in the integrals varies as well. If the magnitude of the spacecraft potential is greater than 100 V, the entire ion line is included in the moments integral without any attempt to partition <100 eV and >100 eV ions.

Anisotropy Measure

The anisotropy measure A is a measure of the variation in fluxes as a function of pitch angle α:

$$A = \frac{T_{perp}}{T_{para}} - 1 \tag{40}$$

This measure comes out of the study of interactions between particles and plasma waves [e.g., *MacDonald et al.*, 2008; *Blum et al.*, 2009]. It was derived originally by *Kennel and Petschek* [1966] as a special case for a bi-Maxwellian distribution. If the phase space distribution is greater at α = 90º than at α = 0º, A is positive. If A is positive, electron whistler waves that are resonant with electrons on the tail of the distribution (e.g., those measured by MPS-HI) may be generated if additional conditions are met [*Kennel and Petschek*, 1966; *MacDonald et al.*, 2008]. In the case of positive ions, if A is positive and sufficiently large, electromagnetic ion cyclotron (EMIC) waves will be generated [*Kennel and Petschek*, 1966; *Blum et al.*, 2009]; if A is negative, magnetosonic waves may be generated [*Kennel and Petschek*, 1966].

The anisotropy measure A is calculated separately for each of the three energy ranges and each species.

3.5 Algorithm Output

The outputs of the MPS-LO and MPS-HI moments algorithms are defined in separate tables (Table 6 and Table 7). Output quantities are single-precision floating point except for Julian date (double precision floating point) and flags and version numbers (integers).

Table 6. Level 2 Outputs (including Quality Flags) of SEISS MPS-LO Moments and Level of Spacecraft Charging Algorithm

Data Type	Refresh	Number of values	Units
MPS-LO Electron and Ion Density Moments and	1 min	2	cm^{-3}
MPS-LO Electron and Ion Temperature Moments	1 min	4	keV
MPS-LO Electron and Ion Anisotropy Measures	1 min	2	Unitless (temperature ratios)
Spacecraft Frame Potential	1 min	1	V
Differential Barrier Potential	1 min	1	V
MPS-LO Pitch Angles	1 min	12	degrees

Data Type	Refresh	Number of values	Units
Corrected MPS-LO Channel Center Energies	1 min	Electrons: 15 Ions: 15	keV
Flag: Ion Line Used to Determine Spacecraft Potential	1 min	1	0 = not used, 1 = used
Flag: Temperatures Used to Determine Spacecraft Potential	1 min	1	0 = not used, 1 = used
Flag: Trapped Photo- and Secondary Electrons Removed	1 min	1	0 = not detected, 1 = detected and removed
Flag: Missing Magnetic Field Data	1 min	1	0 = data not missing, moments calculated 1 = data missing, moments not calculated
Flag: Missing Electron Flux Data Flag: Missing Ion Flux Data	1 min 1 min	1 1	0 = data not missing, moments calculated 1 = 1 flux value missing in at least one energy channel, moments calculated 2 = more than 1 flux value missing in at least one energy channel, moments not calculated
Time	1 min	1 (start of period)	Seconds since J2000 epoch

Table 7. Level 2 Outputs (including Quality Flags) of SEISS MPS-HI Moments Algorithm.

Data Type	Refresh	Number of values	Units
MPS-HI Electron and Proton Density Moments	1 min	4	cm^{-3}
MPS-HI Electron and Proton Temperature Moments	1 min	8	keV

Data Type	**Refresh**	**Number of values**	**Units**
MPS-HI Electron and Proton Anisotropy Measures	1 min	4	Unitless (temperature ratios)
MPS-HI Pitch Angles	1 min	5	degrees
Flag: Missing Magnetic Field Data	1 min	1	0 = data not missing, moments calculated 1 = data missing, moments not calculated
Flag: Missing Electron Flux Data Flag: Missing Proton Flux Data	1 min 1 min	1 1	0 = data not missing, moments calculated 1 = 1 flux value missing in at least one energy channel, moments calculated 2 = more than 1 flux value missing in at least one energy channel, moments not calculated
Time	1 min	1 (start of period)	Seconds since J2000 epoch

4.0 TEST DATA SETS AND OUTPUTS

4.1 Simulated/Proxy Input Data Sets

Five simulated or proxy data sets have been used to verify and validate the algorithm performance:

1. Theoretical Maxwellians have been used to verify correct units and to check the effect of energy resolution and range on the calculated moments.

2. DMSP SSJ/4 data have been used to compare density and temperature from the moments algorithm to results of curve fits for published cases.

3. LANL MPA fluxes have been resampled in energy and pitch angle to mimic the MPS-LO measurements, and the resulting moments and spacecraft charging identifications have been compared with those calculated by the LANL algorithm.

4. Partial moments have been calculated from GOES 13-15 MAGED and MAGPD fluxes and Magnetometer-derived pitch angles.

5. Partial densities and temperatures have been calculated from the GOES 14 EPEAD relativistic electron channels using curve fits and the relativistic moments algorithms in order to validate the latter.

A sampling of these results is shown in the next section.

4.2 Output from Simulated/Proxy Inputs Data Sets including Error Estimates

Theoretical Maxwellians

Using theoretical Maxwellians, a trade study was conducted to compare the LANL quadrature method [*Thomsen et al.*, 1999], as adapted to the MPS-LO measurements, to the *Twomey* [1977, pp. 33-35] quadrature method. The energy dimension was evaluated. The LANL method sets the bin limits at the channel edges and treats the fluxes as flat across the bin. The Twomey method assumes a linear variation in fluxes across the bin and sets the bin limits at the channel centers. The motivation for the study was the concern that a quadrature method that works well for the high-energy-resolution MPA instrument might not work as well for the coarser MPS-LO spectral sampling.

The comparison was performed for a 0.03-30 keV energy range, 15 energy channels, and an isotropic Maxwellian distribution with a number density of 1000 cm^{-3}. The

temperature was varied from 0.1 to 10.0 keV. The results are summarized in Table 8. The results of the trade study also indicate the effect of limited energy range and sampling on the moments calculations.

Table 8. Comparison of moments calculation for an isotropic Maxwellian of n = 1000 cm^{-3} and a range of temperatures, using two quadrature methods.

T, true (keV)	n, LANL (cm^{-3})	T, LANL (keV)	n, Twomey (cm^{-3})	T, Twomey (keV)
0.1	948.2	0.112	958.8	0.121
0.3	1007.	0.317	1040.	0.346
0.5	1015.	0.524	1052.	0.572
1.0	1020.	1.04	1058.	1.14
3.0	1022.	3.12	1061.	3.40
5.0	1022.	5.18	1047.	5.32
10.0	973.1	9.10	912.5	7.48

Before starting the study, it was assumed that the Twomey method, with its first-order correction, would give better results than the LANL method, given the relative coarseness of the MPS-LO energy sampling compared to the LANL MPA instrument. However, the results were to the contrary of this expectation. Both methods tended to overestimate the temperature and density, but the Twomey method overestimated them more. This may be due to the fact that Maxwellian distributions are ‘concave up’ in the linear-linear space in which the integration occurs, so a linear approximation to the spectral variation tends to overestimate the integral.

The results also show that when the temperature is relatively low (0.1 keV) or high (10 keV), the spectra are not captured as well by the instrument measurement range. For a 0.1 keV Maxwellian, the temperature is overestimated as for higher temperatures (the tail is adequately captured) but the density is underestimated due to the 0.03 keV low energy cutoff. For a 10 keV Maxwellian, both the temperature and density are underestimated since the high energy tail is cut off at 30 keV. Regardless, at the ends as well as in the middle of the tested temperature range, the LANL quadrature method gives comparable or better results than the Twomey method. The conclusion of the study is not to change the quadrature method.

DMSP SSJ/4 Proxy Data

SSJ/4 measures precipitating electrons and ions from the DMSP spacecraft in low-earth orbit. The SSJ/4 instrument has an energy range of 0.03-30 keV in 19 logarithmically-spaced energy channels with a single field-of-view pointed toward the zenith. We show an example here of a classic observation of cusp precipitation at low altitudes that has

been studied before [*Newell and Meng*, 1988, 1995]. A spectrogram of the number fluxes is shown in Figure 7.

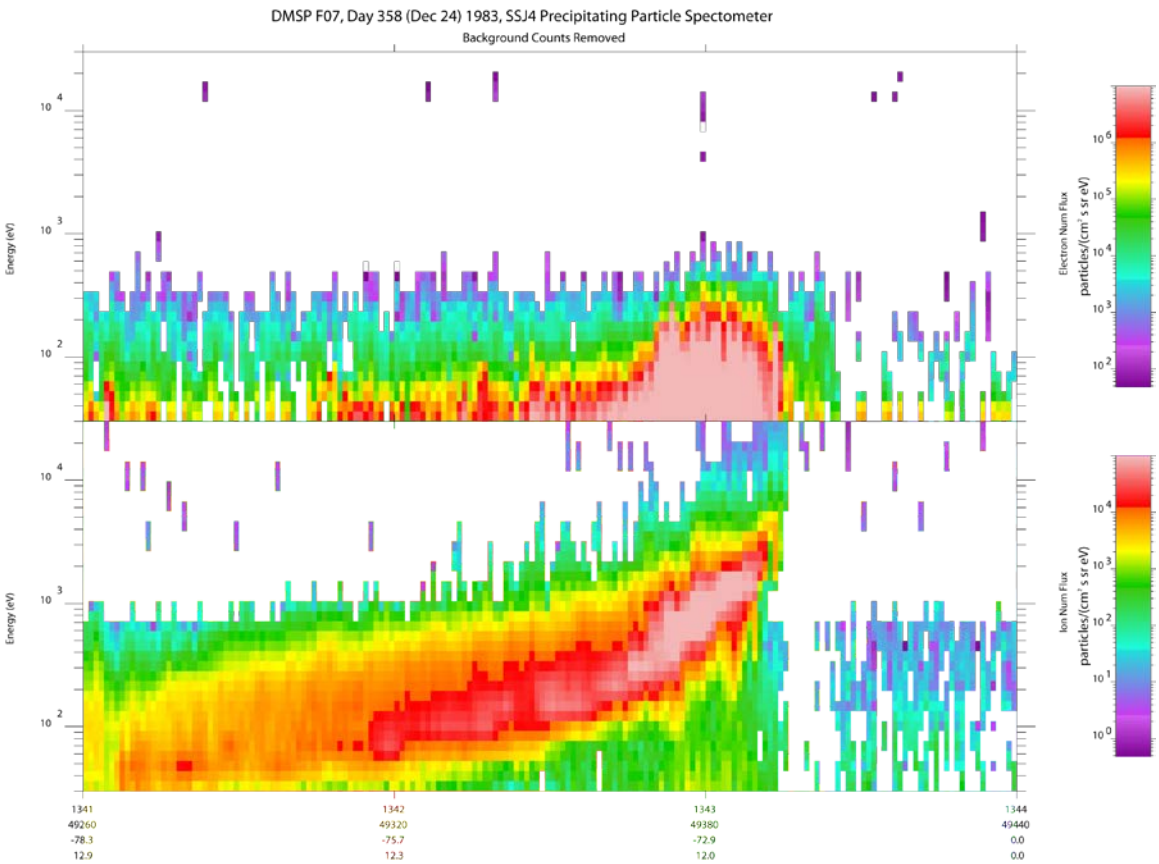

Figure 7. Spectrograms of (top) electron and (bottom) ion number differential fluxes measured by SSJ/4 on DMSP F7, 24 December 1983, 1341-1344 UT.

Due to the very small loss cone at the magnetopause, the equivalent Maxwellian distribution calculated from DMSP data is given by [*Hill and Reiff*, 1977]:

$$f = \left(\frac{T_{par}}{T_{perp}} n\right)\left(\frac{m}{2\pi k T_{par}}\right)^{3/2} \exp\left(-\frac{m v_{par}^2}{2kT_{par}}\right)\exp\left(-\frac{E}{kT_{par}}\right)$$

Therefore, the derived number density is in theory the density of the source population scaled by ratio of the parallel to the perpendicular temperatures in the source population (at the magnetopause). The perpendicular temperature cannot be determined from the DMSP measurements. Note that typical field-aligned velocities in the cusp are much smaller than electron thermal velocities, so the electron velocity can be taken to be zero in the above expression. Due to the assumption of isotropy, the field-aligned proton

velocity cannot be determined from the first-order moment integral. Therefore, the ion temperatures derived here both from the moments integrals and from a two-parameter Maxwellian fit may include contributions of field-aligned flow velocities. The results of the moments calculations for the spectra in Figure 7 are shown in Figure 8. Three sample spectra are shown in Figure 9.

A significant departure between the densities and temperatures calculated using the moments integrals and using curve fits is an indication that the Maxwellian model is not good for the spectrum in question. According to *Newell and Meng* [1988], the cusp corresponds to the region of highest electron and ion density, between 1342:47 and 1343:15 UT. Where the counts are sufficiently great (i.e., in the cusp), the agreement between the integral and Maxwellian fit determinations of electron density and temperature is good at times (Figure 8). In contrast, within the cusp the agreement between the integral and Maxwellian fit determinations of the ion density and temperature is poor (Figure 8).

Where the ion agreement is poor, as at 1343:08 UT in the cusp, the ion spectra are poorly represented by Maxwellians due to their low energy cutoff (Figure 9) characteristic of recently-opened field lines [*Newell and Meng*, 1995]. Where the results agree reasonably well, as at 1342:00 UT in the ions and 1343:08 UT in the electrons, the spectra are adequately represented by Maxwellians, though there is still a low energy ion cutoff downstream in the cusp plume (Figure 9). The moments calculated using the integrals are generally smoother, which is one indication of a more reliable calculation, and are not model-dependent, which is often a pitfall for a curve fit. These results represent a successful partial validation of our implementation of the moments algorithm, including the proper handling of physical units in the conversion of flux to moments.

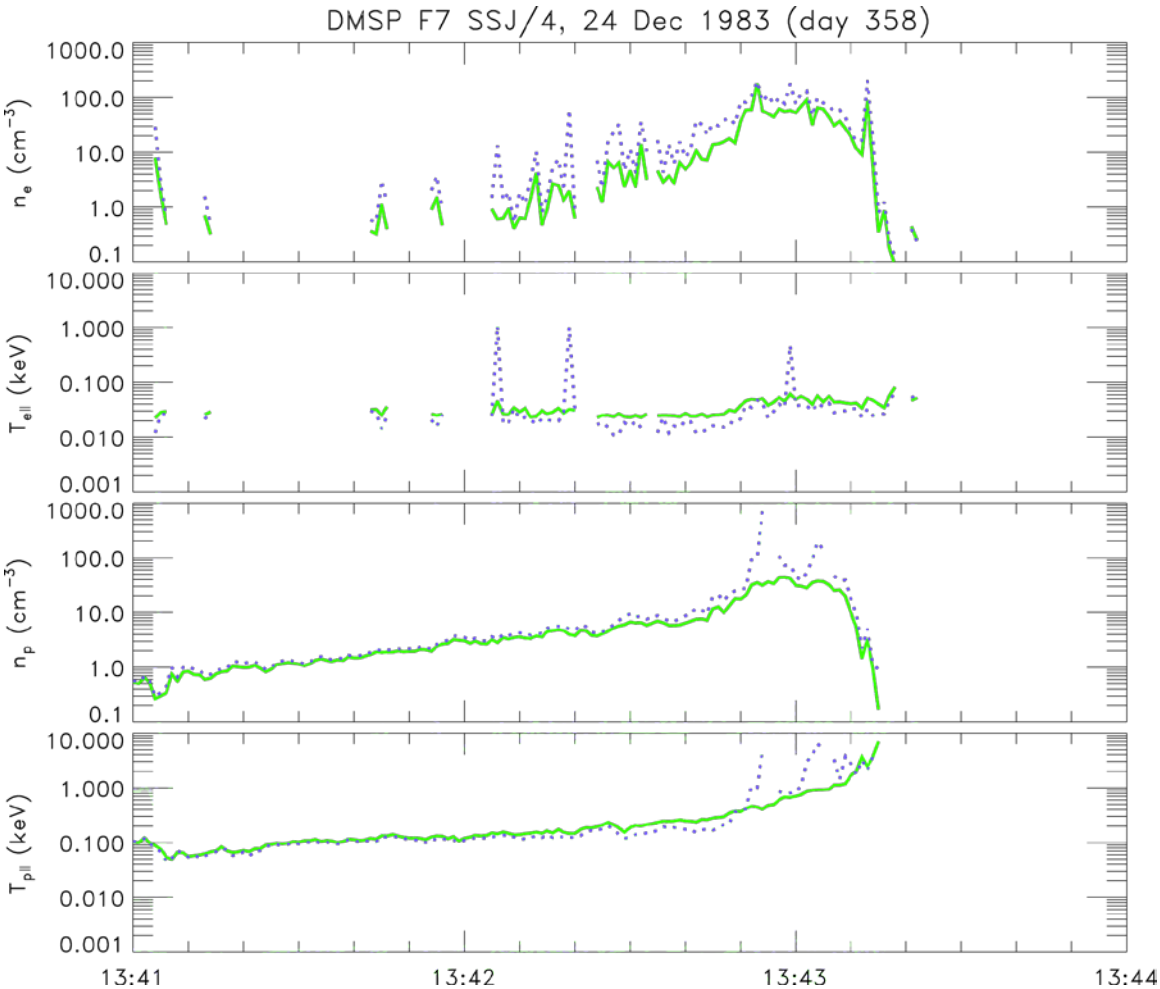

Figure 8. Density and temperature moments from the DMSP flux measurements shown in Figure 7. The dotted lines represent moments calculated from two-parameter Maxwellian fits to the spectra, and the green lines represent the moments calculated using the integrals.

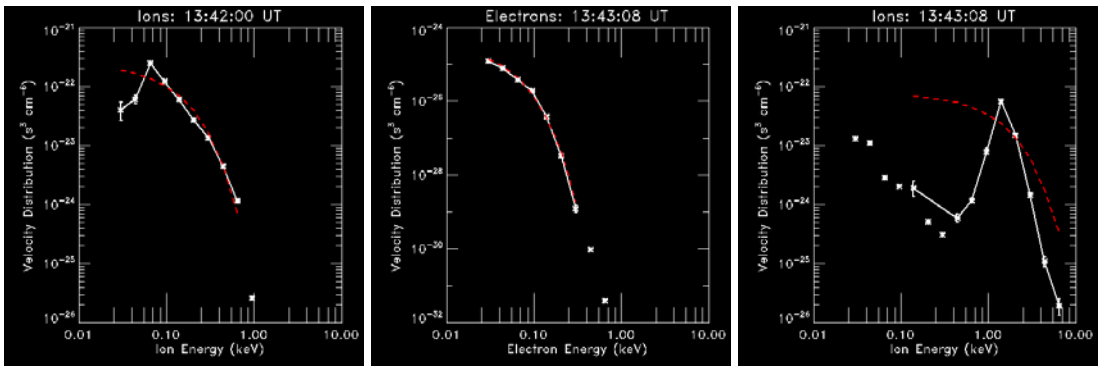

Figure 9. Sample spectra from 1342:00 UT (ions) and 1343:08 (electrons and ions) showing measured velocity distributions (white) and two-parameter Maxwellian fits to these distributions (red).

LANL MPA Proxy Data

The GOES-R moments and spacecraft charging algorithm is based on the moments algorithm for the LANL MPA instrument flying on geosynchronous satellites [*Bame et al.*, 1993; *McComas et al.*, 1993; *Thomsen et al.*, 1999]. Therefore, a comparison of the moments calculated by LANL and moments calculated using the GOES-R algorithm on subsampled MPA data is in order. LANL produces CDF files that contain both the complete ion and electron distributions at 86-s intervals and the moments calculated from them. Dr. Michelle Thomsen of LANL has provided some CDF files as well as much assistance in using the data and understanding the LANL moments algorithm. We chose to derive proxy data from the MPA instrument on LANL-02A because all of its channel electron multipliers function (providing more angular samples) and it has the complete energy range due to properly functioning high-voltage power supplies.

The MPA FOV integrated over a spin cycle resembles a torus that is symmetric about an axis pointing to the center of the earth [*McComas et al.*, 1993]. Therefore, it has a hole where the MPS-LO FOV would be. This requires that the MPA data be subsampled by pitch angle rather than by physical overlap. The pitch angles of the MPA data are calculated using the symmetry axes of the particle distributions derived by eigenanalysis. The electron symmetry axes are generally more dependable (less noisy) [*Thomsen et al.*, 1999], but not always, so we use the ion or electron symmetry axes based on which has a smaller variance within a ten-sample (860 s) window.

An example is shown from 26 October 2003, a quiet day (*Kp* between 1 and 2+ until the last six hours when it was 3+ and 4-) with some spacecraft charging (Figure 10). The electron and ion symmetry axes are shown in Figure 11, along with the derived center pitch angles for the proxy MPS-LO zones.

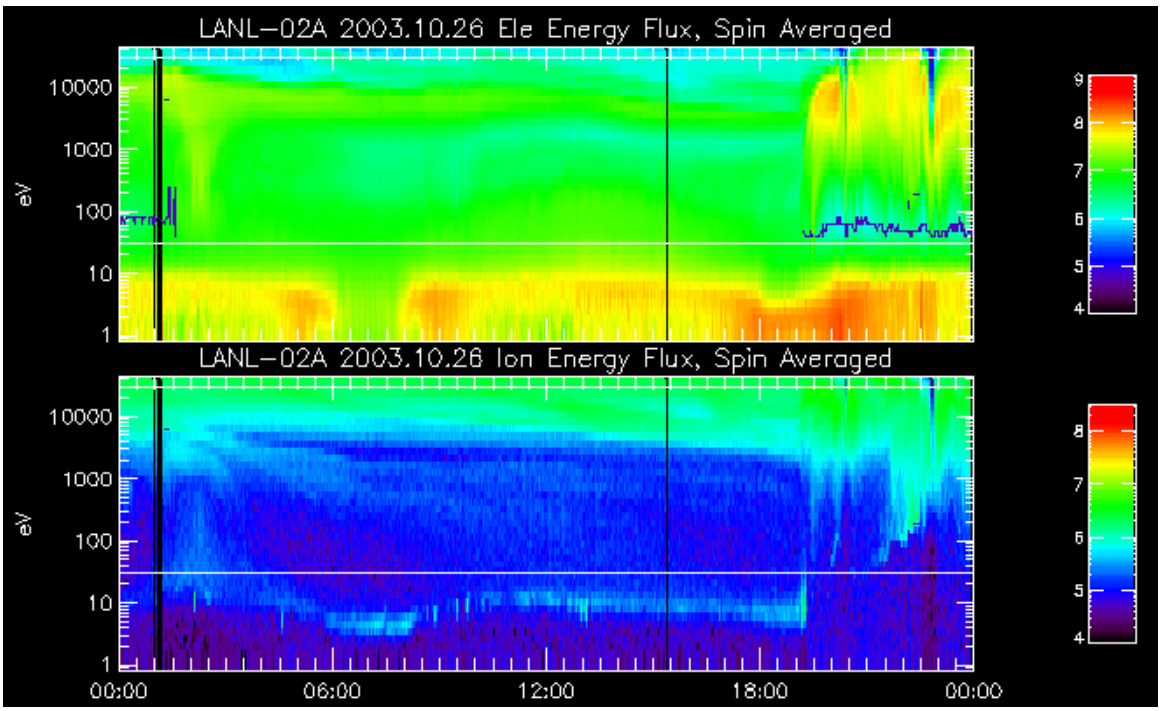

Figure 10. Spectrograms of spin-averaged electron and ion energy differential fluxes measured by the LANL MPA instrument on 26 October 2003. The horizontal axis represents universal time. The vertical axis represents the energies of the particles in electron volts (eV). The color scale represents the base-10 logarithm of the energy flux in units of eV cm^{-2} s^{-1} sr^{-1} eV^{-1}. MPA data provided courtesy of M. Thomsen, Los Alamos National Laboratory.

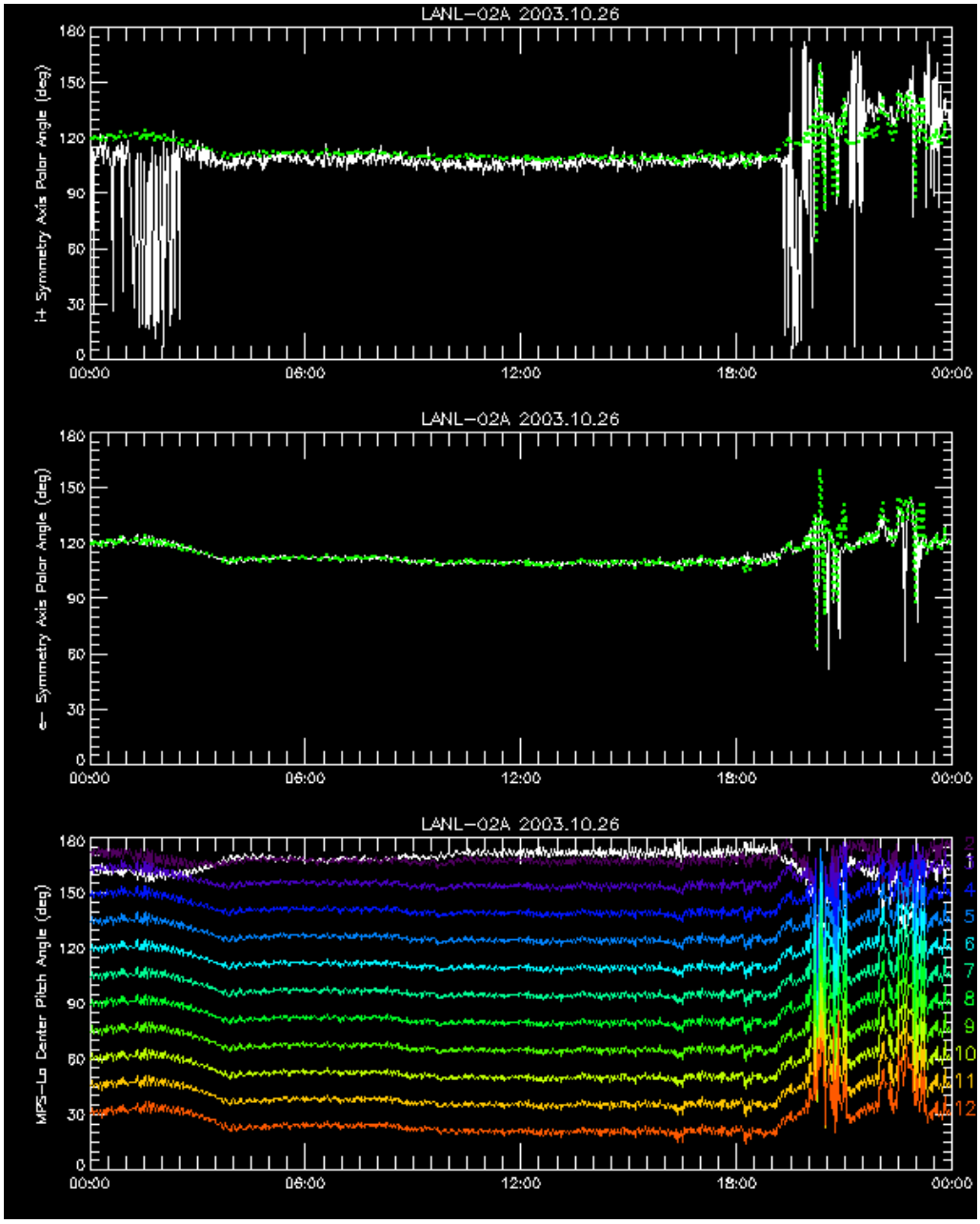

Figure 11. Ion and electron symmetry axes derived from LANL-02A MPA fluxes measured on 26 October 2003, and the proxy pitch angles derived from them. In the top and middle panel, the white trace indicates the symmetry axis for the given species and the green trace indicates the 'best' symmetry axis determined by taking the axis with the lowest variance in a 10-sample (~860 s) period.

The density and temperature moments for 26 October 2003 are shown in Figure 12 for ions and in Figure 13 for electrons. The anisotropy measure *A* is also shown. Three separate calculations are represented: the original LANL moments calculated using the

full resolution data; moments calculated using the GOES-R algorithm with proxy data at full energy range and resolution and degraded angular resolution; and GOES-R moments calculated from proxy data with degraded energy range and resolution and degraded angular resolution.

The similarity between the LANL-calculated ion moments and those with full energy range and resolution but degraded angular resolution indicates that the angular resolution does not drive performance in this case (Figure 12). Significant discrepancies are evident in the temperatures and anisotropy measure, but not the number density, when the upper end of the energy range is reduced from 40 keV to 30 keV. (The lower end of the energy range is 130 eV in all three cases.) The reason for this is that the number density is dominated by the lowest energy ions, but the temperature is strongly affected by the highest energy fluxes. The 30-40 keV range measured by MPA but not MPS-LO is characterized by ring current fluxes that will raise the partial temperature if they are included (see Figure 10 and Figure 14).

In contrast, the electron moments show larger discrepancies between the LANL-calculated moments (30 eV – 40 keV) and the two proxy sets (30 eV – 30 keV) (Figure 13). The lower end of the energy range is 30 eV in all three cases. An example of a quiet-time spectrum from 1211:56 UT is shown in Figure 14. If the arguments used to explain the ion moment similarities and differences are correct, then the electron moments should agree very well because the electron density and temperature contribution between 30 and 40 keV should be negligible. Based on Figure 14, the discrepancies seem to be due rather to the proxy fluxes being systematically low. This could be due to a real angular sampling difference in the electron fluxes that is not present in the ion fluxes, or an artificial sampling difference introduced at some point in the creation of the proxy data.

Results of the spacecraft charging algorithm are shown in Figure 15. The example used is the set of measurements from 2 November 2003, shown in Figure 3. The top panel shows the identification of the potential barrier (differential charging signature) in the electron fluxes for both the MPA and MPS-LO energy resolution. The differences between the two are minor.

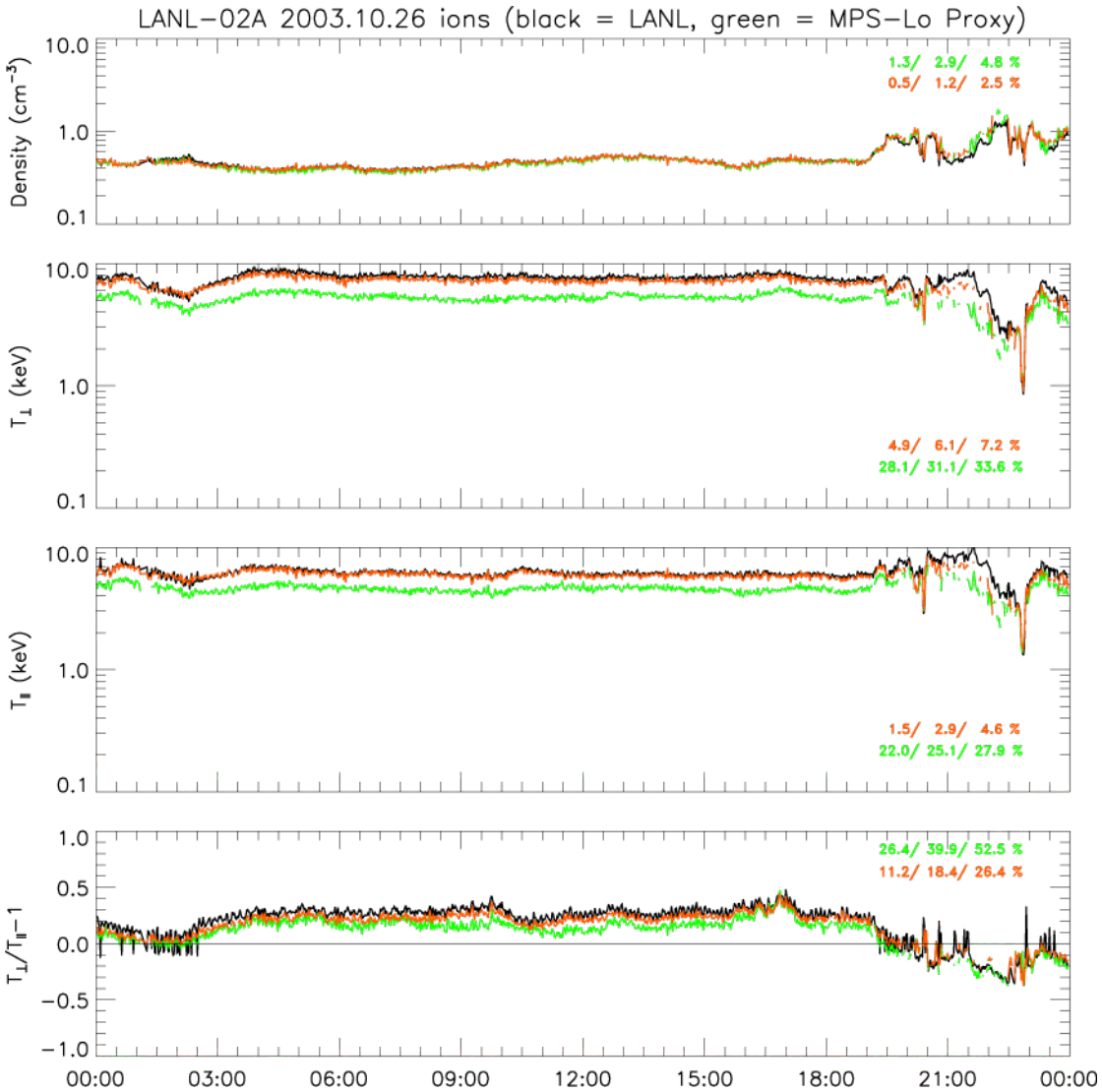

Figure 12. Ion moments from LANL-02A MPA, 26 October 2003. The black traces are the moments from the CDF file, calculated by LANL. The orange traces represent the moments calculated from proxy data with MPA energy resolution and MPS-LO angular resolution. The gree traces represent the moments calculated from proxy data with MPS-LO energy and angular resolution. The numbers at the upper right of each panel represent the lower quartile, median and upper quartile of the absolute differences between the LANL moments and the proxy moments (color-coded).

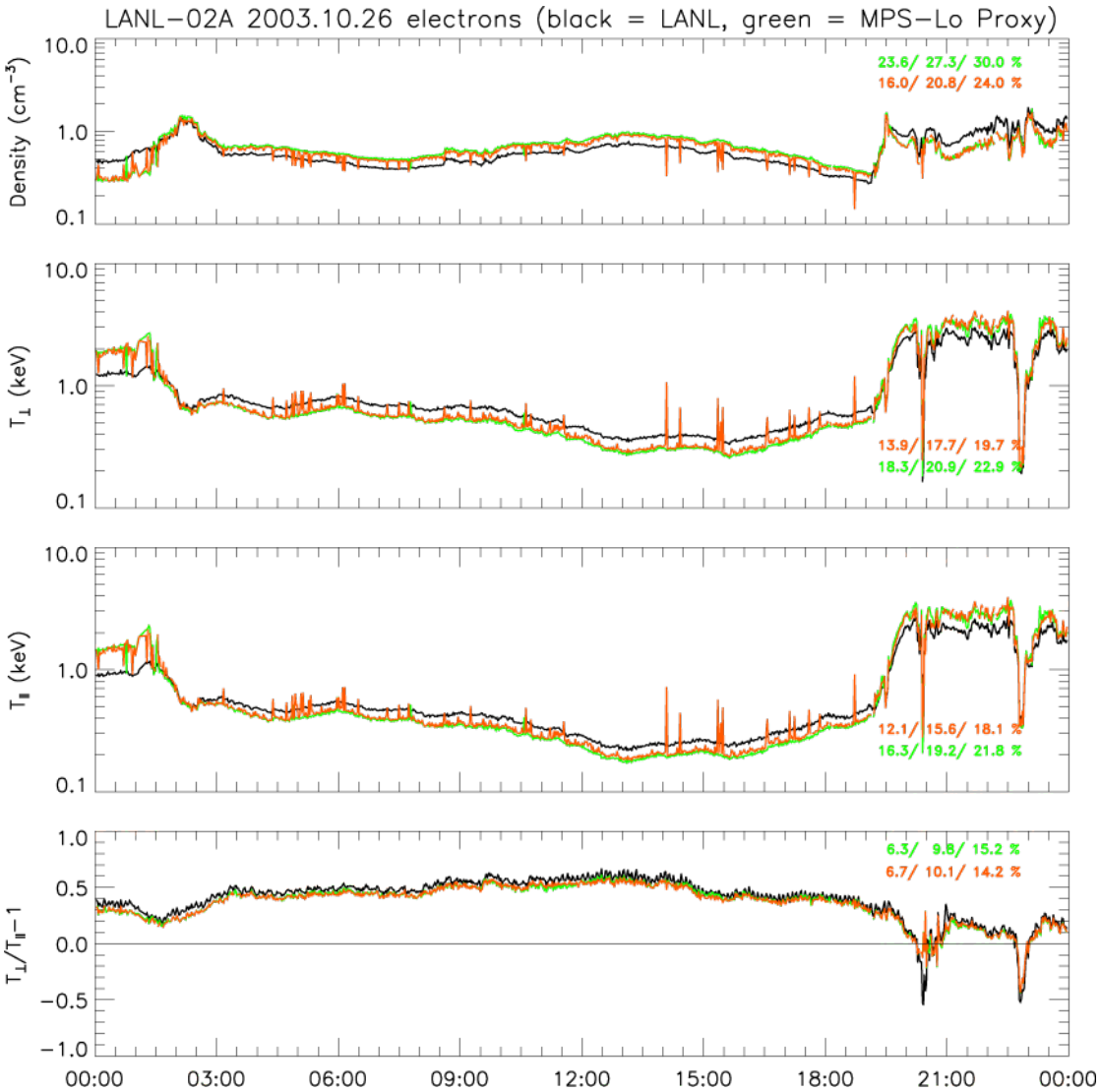

Figure 13. Electron moments from LANL-02A MPA, 26 October 2003. The black traces are the moments from the CDF file, calculated by LANL. The orange traces represent the moments calculated from proxy data with MPA energy resolution and MPS-LO angular resolution. The gree traces represent the moments calculated from proxy data with MPS-LO energy and angular resolution. The numbers at the upper right of each panel represent the lower quartile, median and upper quartile of the absolute differences between the LANL moments and the proxy moments (color-coded).

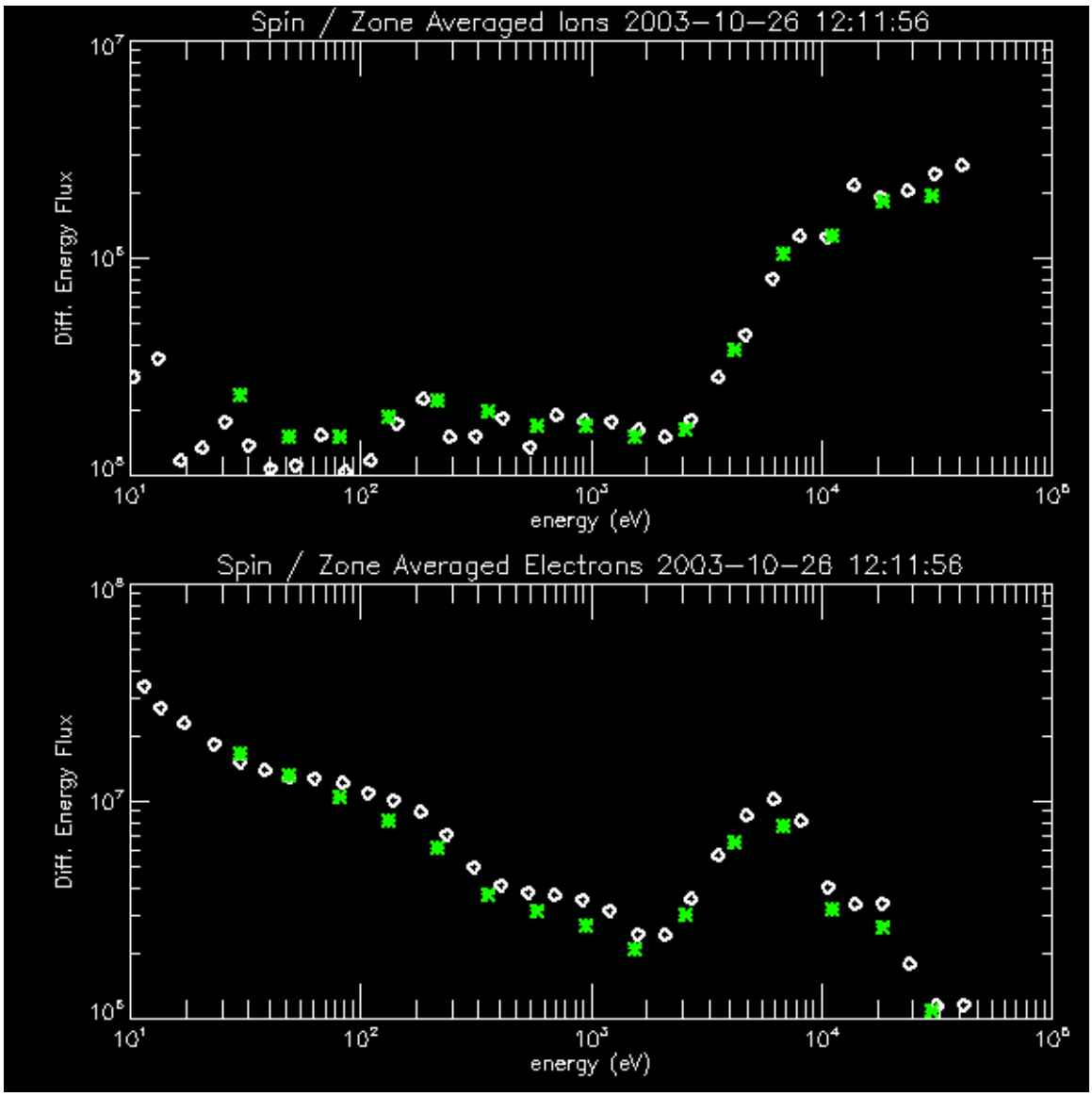

Figure 14. Spin-averaged ion and electron differential energy flux spectra from 26 October 2003, 1211:56 UT. The white diamonds represent the MPA data and the green asterisks represent the subsampled proxy data. Note that energy flux is a scaling of number flux that is linear with energy. Therefore, the highest energies are emphasized in energy flux.

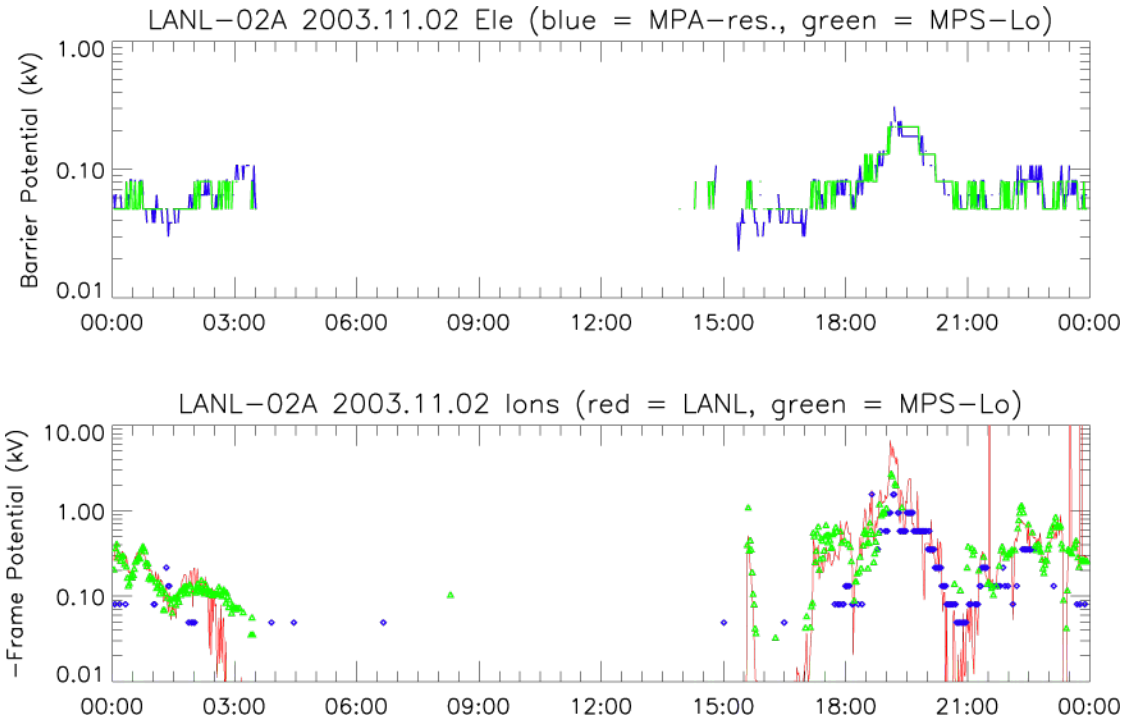

Figure 15. Estimates of spacecraft charging on LANL-02A from 2 November 2003 (see Figure 3 for the spectrogram of the fluxes). The upper panel shows the barrier potential calculated from the electron fluxes. The green trace is at MPA energy resolution and the blue trace is at MPS-LO energy resolution. The lower panel shows the negative of the frame potential derived from the ion data or from the electron temperature moment. The blue diamonds represent the potential derived from the ion line in the proxy data. The green triangles represent the potential derived from the electron temperature from the proxy data. The red line represents the potential from the LANL CDF file.

The bottom panel of Figure 15 shows three separate determinations of the frame potential: the original LANL results, the identification of the ion line from the proxy data, and the estimate using the electron temperature from the proxy data in the absence of an automatically-detectable ion line. One important difference between the LANL and proxy results is that the LANL estimation combines two partial moments: the 30 eV – 40 keV temperature, and an estimate of the cold electron density derived from the 1-100 eV ion density, which GOES-R will not have. Despite these differences, the results are in reasonable agreement. Again, as emphasized elsewhere in this ATBD, the relation between electron temperature and frame potential will have to be evaluated anew for GOES-R.

Partial Moments from GOES-13 MAGED Electron Fluxes and Magnetometer-derived Pitch Angles.

The GOES-R moments algorithm has been used to calculate partial moments from the 30-600 keV electron fluxes measured by the MAGED instrument on GOES-13. Pitch

angles derived from the three-axis fluxgate magnetometer on GOES-13 have been used in these calculations. The physical behavior of one year of GOES-13 density and temperature with respect to solar wind speed and solar wind number density has been studied in depth by *Hartley et al.* [2014]. Recognizing that the temperature moment is inversely proportional to number density, this paper also studied the behavior of energy density (the product of number density and temperature). For details, please refer to this paper.

Relativistic Electron Moments from GOES

As a proxy set for the highest energy electrons, we derive differential fluxes from the GOES 14 EPEAD integral electron channels. Because of the large EPEAD FOVs, these fluxes are assumed to be omnidirectional. However, the essential need for testing the relativistic moments integrals is satisfied

The process and results are captured in Figure 16. The proxy data are from the period from 6 April through 11 April 2010. The top panel shows the magnitude of the magnetic field from the GOES 14 magnetometer. The second panel shows the integral electron fluxes in the >0.8, >2 and >4 MeV channels from EPEAD. This period was chosen because the >4 MeV fluxes rose above background shortly before 12 UT on 6 April. Using the non-linear maximum likelihood retrieval method of *O'Brien* [2010], we fit the weighted sum of a relativistic Maxwellian, a power law and an energy exponential to the integral flux measurements using the full energy-dependent geometrical factors. The third panel shows the results of this fit: differential fluxes at fixed energies. The weights for each analytical form are plotted in the fourth panel. This shows that, after the >4 MeV fluxes rise above background, the relativistic Maxwellian dominates, the energy exponential contributes significantly, and the power law does not contribute at all to the fit.

The fifth panel provides the validation of the relativistic moments integrals. The partial number density and temperature from the relativistic Maxwellian fit are plotted in black and orange, respectively. The density and temperature from the moments integrals are overplotted using purple dotted lines. The number density from the fit shows the diurnal variation from the weighting applied to the Maxwellian, while the number density from the integral does not exhibit as pronounced a diurnal variation. The two curves agree well when the relativistic Maxwellian weighting is maximum.

The partial temperatures calculated from the fit and from the relativistic integral agree well and do not exhibit a diurnal variation. This type of behavior was also observed by *Cayton et al.* [1989] in relativistic Maxwellian fits to omnidirectional averages of LANL electron measurements. This lack of a diurnal variation is also apparent in the phase space densities at fixed values of the first adiabatic invariant that are derived from the differential flux fits and measured magnetic field magnitude (bottom panel).

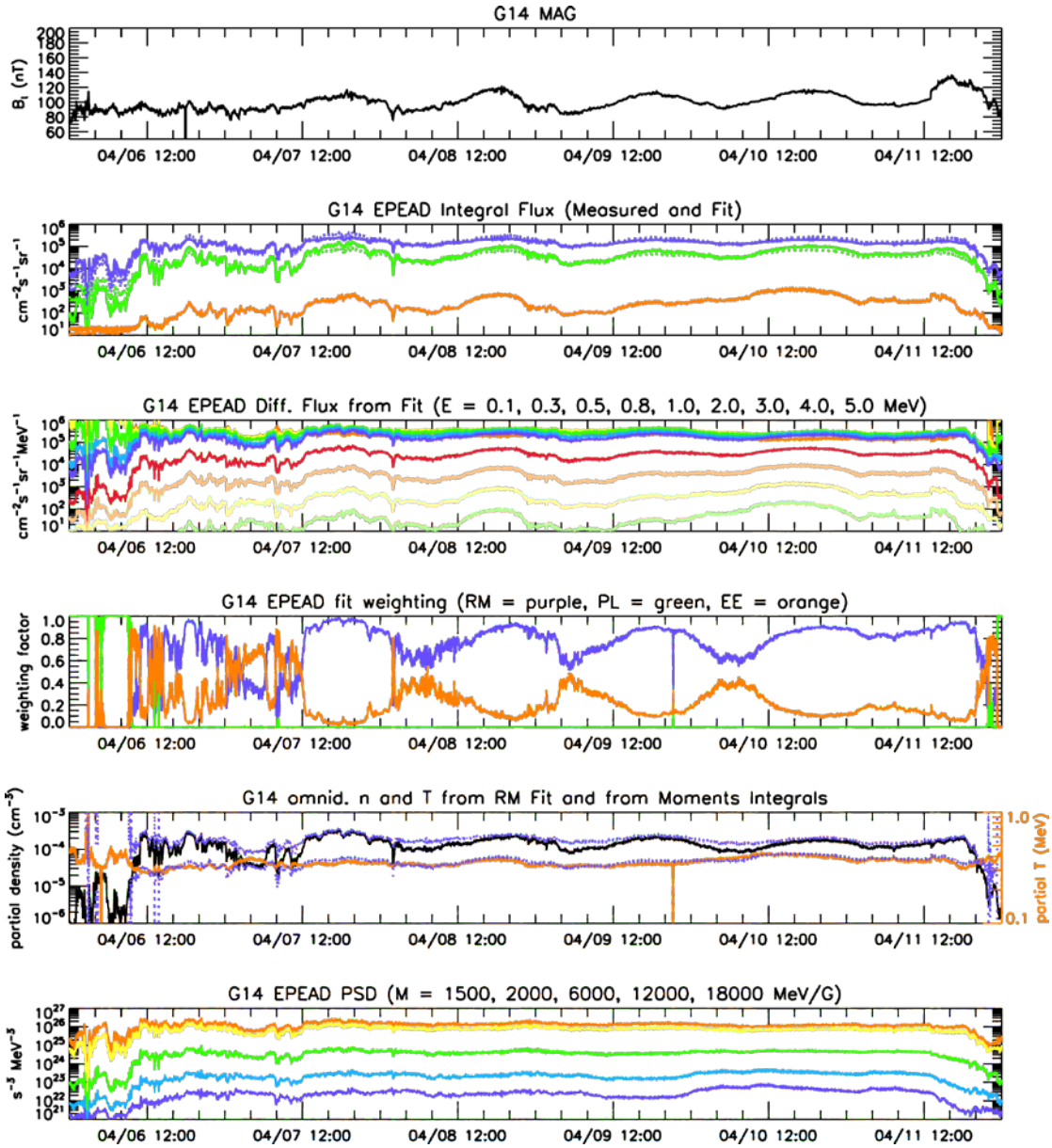

Figure 16. GOES 14 magnetometer (top panel) and EPEAD electron integral flux (2nd panel) measurements from 6-11 April 2010. The third panel shows the differential fluxes fit to the integral flux using a sum of relativistic Maxwellian, power law, and energy exponential analytical forms, whose weights are shown in the fourth panel. The partial number density and temperature from the relativistic Maxwellian fit (solid lines) and the moments integrals (dotted lines) are shown in the fourth panel. The bottom panel shows the phase space density at fixed values of the first adiabatic invariant.

5.0 PRACTICAL CONSIDERATIONS

5.1 Numerical Computation Considerations

The approximations to the moments integrals are defined in section 3. The quadrature method has been adapted from the LANL algorithm [*Thomsen et al.*, 1999] and found to be more accurate than a higher-order method that assumes a linear variation between points as opposed to step changes.

The estimation of spacecraft surface charging level (MPS-LO only) is iterative, involving moments of an omnidirectional average of the measured electron distribution. The number of iterations is limited by a tolerance and a maximum number of iterations, whichever is reached first.

The units of the physical quantities in this algorithm (both calculated and constant) are in the centimeter-gram-second (cgs) system, with the additional use of the kilo-electron-volt (keV) for the kinetic energy and rest masses of the particles as well as their temperatures. The use of cgs units is customary in the field. Because the energy range is so wide, one will often see eV or MeV in the literature for the lowest or highest energy ranges. We use keV throughout to avoid an obvious potential source of error in the calculations and for consistency with the units of the input fluxes. However, be aware that fluxes or temperatures from other sources may be expressed in terms of eV or MeV. See Table 9 for a selection of quantities and their units.

Table 9. Units of selected physical quantities used in the Moments algorithm.

Physical Quantity	**Units**
Particle kinetic energy and rest mass	keV
Velocity	cm s^{-1}
Momentum	keV s cm^{-1}
Differential directional number flux	cm^{-2} s^{-1} sr^{-1} keV^{-1}
Differential directional energy flux	keV cm^{-2} s^{-1} sr^{-1} keV^{-1}
Velocity distribution	s^3 cm^{-6}
Multiplicative factor to convert from number flux to velocity distribution	g s^2 cm^{-2} • (1.602 x 10^{-9} keV/erg)
Phase space density	keV^{-3} s^{-3}
Multiplicative factor to convert from number flux to phase space density	cm^2 keV^{-2} s^{-2}
Number density	cm^{-3}
Temperature (kT)	keV
Anisotropy	unitless

5.2 Programming and Procedural Considerations

The algorithm is implemented in an object-oriented fashion. In the first version, the MPS-HI and MPS-LO algorithms are not coupled. However, in the event that they are coupled after on-orbit validation, the MPS-HI moments should be calculated first.

5.3 Quality Assessment and Diagnostics

See Table 6 and Table 7 for a list of the quality flags set by the algorithm.

5.4 Exception Handling

It is assumed that bad or missing flux values are indicated by a standard fill value. In any energy channel (for a given species), i.e. in a pitch-angle distribution at constant energy, at most one flux value may be missing, or the moments are not calculated for that species. If the missing flux value is at the lowest or highest pitch angle, the fill value is replaced by its nearest neighbor for calculating the moments. Otherwise, it is replaced by the linear interpolation (vs. pitch angle) of its two neighbors.

If a telescope or zone is known to have problems (like GOES 15 MAGED Telescope 7 during 2010), the algorithm can be forced to omit it from the calculation regardless of whether fill values are used. This choice is indicated by flags in the telescope or zone calibration table. This is a serious condition that may amount to a failure of the instrument. Even an occasional missing flux value is a problem, and the ability to handle it adds significant complexity to this algorithm. A more serious failure than the situations envisaged here is out of the scope of this development and will have to be dealt with specifically if it arises.

5.5 Algorithm Validation

Prior to delivery, the best validation of the algorithm itself comes from the comparison with LANL moments shown in section 4. This work shows that, when processing the same event with fluxes measured by a different instrument, the results will be similar, with differences explained mostly by the different energy ranges and resolutions of the instrument.

The best opportunity for validating the algorithm prior to the launch of GOES-R has been to use it to calculate partial moments from GOES 13-15 MAGED and MAGPD. The physical behavior of one year of GOES-13 electron moments has been studied in depth by *Hartley et al.* [2014].

Ultimately, the moments are only as good as the fluxes. Therefore, any effort to validate the Moments algorithm will by necessity involve the validation of the fluxes.

6.0 ASSUMPTIONS AND LIMITATIONS

6.1 Performance

The nature of the measurement precludes any accurate calculation of the first-order velocity moment, the drift velocity. Therefore it is assumed to be identically zero. The one possible exception to this is the ion flow velocity in the magnetosheath or low-latitude boundary layer, which comprise about 0.7% of geosynchronous measurements [*McComas et al.*, 1993]. In these regions, the drift velocity would be comparable to or greater than the mean thermal velocity.

Due to sparse angular sampling, we must assume that all variation is in pitch angle (i.e., gyrotropy) and energy, ignoring azimuthal variations. This precludes any determination of velocity in the magnetosheath from MPS-LO data except along the field line. Because of the relative sparseness of MPS-HI pitch angle sampling, the MPS-HI PAD is forced to be symmetric about 90 deg.

MPS-LO does not distinguish p+ from other ions (e.g., O+). This is true of all electrostatic analyzers (e.g., LANL MPA). This will present an issue for measuring the ring current during disturbed periods. However, the gap in energy coverage between MPS-LO and MPS-HI ion measurements may present a more serious problem. This is one reason why the algorithm is producing partial moments; their accurate combination in a 'total' moment will depend on the conditions being measured.

The spacecraft charging algorithm assumes an idealized (spherical) spacecraft sheath. This is the assumption that the LANL moments algorithm makes [*Thomsen et al.*, 1999]. It is probably the only practical approach for a near-real time operational algorithm. Depending on spacecraft geometry near the MPS-LO, pitch angle distributions could be distorted by spacecraft charging, both total and differential. The full magnitude of this error will be unknown.

This error-prone situation is flagged so that the user can be appropriately cautious in using the moments. Quality flags (Table 6 and Table 7) identify whether the ion line has been identified, whether the spacecraft potential has been calculated using electron temperatures, and whether trapped secondary electrons or photoelectrons have been removed.

6.2 Assumed Sensor Performance

The following assumptions are made about sensor performance and characterization:

1. MPS-LO, MPS-HI and MAG will meet their performance requirements. Implicit in this is the assumption that the MPS-HI channels will be sufficiently narrow to be

accurately represented as differential channels. This is not an issue for the MPS-LO channels.

2. The reported MPS-HI channel centers and geometrical factors will be derived from "bowtie" analysis, in order to minimize the uncertainty due to spectral variability.

3. Sensor characterization data used by the Moments algorithms reside in calibration processing parameter files and telescope / zonal calibration files with standardized names that are distinguished by version number.

4. One-minute averages of the GOES-R MAG magnetic field will be available in real-time in spacecraft body reference frame (BRF) coordinates with the same time stamp.

5. The spacecraft eclipse flag required for EXIS processing (flare detection) will be available to the moments algorithm as well.

6.3 Pre-Planned Product Improvements (P3I)

The suggested improvements here are best addressed with on-orbit data and therefore are relegated for consideration to the post-launch validation phase.

6.3.1 Validation of Spacecraft Potential Estimate based on Temperature

Determination of spacecraft potential using moments requires validation against the direct ('ion line') method during the post-launch validation phase. A direct observation of the 'ion line' is not always possible (since it requires a sufficiently dense population of cold ions). The inferred method depends on a statistical relation between moments (temperature) and the 'ion line' signature. Separate relations are derived for eclipse and non-eclipse conditions. As noted in section 3.4.2, the correlation between electron temperature and spacecraft charging needs to be evaluated after launch for each GOES-R+ satellite. It is not expected that even the functional relation developed for the LANL satellites will be the same for GOES-R, let alone the coefficients.

The relation that is currently implemented was derived using the partial moments from the LANL instrument that is equivalent to the MPS-LO. There may be an improvement in the correlation if a combined temperature from the MPS-LO and MPS-HI is calculated. The current code for the MPS-LO moments and spacecraft charging has input variables for the MPS-HI parallel and perpendicular temperatures, from which it can calculate an omni-directional average temperature. However, the current version sets these variables to zero since any improvement in the correlation needs to be validated before the MPS-LO and MPS-HI moments calculations are linked in this manner with the associated complications.

6.3.2 Deriving Field-Aligned Flow Velocity in the Magnetosheath

Once we have measurements in the magnetosheath from GOES-R+, it may be worthwhile to explore deriving the field-aligned flow velocity from the MPS-LO measurements. The field-aligned proton velocity may be determined from the first-order moment integral:

$$v_{para} = \frac{2\pi m}{n} \int f_v(\alpha, v) v^3 \cos(\alpha) \sin(\alpha) d\alpha \, dv \tag{41}$$

If the field-aligned flow velocity can be successfully calculated, it can then be explored whether accounting for it would significantly affect the calculation of the temperature. Proxy data derived from the LANL MPA cannot be used to test this possibility because there is a 'hole' in the MPA angular coverage where the MPS-LO angular coverage would be, and vice versa. In the work of *McComas et al.* [1994], none of the four viewing quadrants (north, south, west, and east) is directed radially outward like MPS-LO. Proxy data from other missions could be misleading if they are not measured near L = 6.6 during a strong compression event that could cause a geosynchronous magnetopause crossing.

6.3.3 Estimating Cold Ion Density from the Ion Line

A cold ion density can be derived from the counts in the ion line [*DeForest*, 1972]. The quality of this calculation is affected by the energy resolution of the instrument. It would require some assumption about the temperature of the cold ion population. Depending on the nominal center energy and energy width of the channel in which the ion line is observed, there will be mixing of the < 100 eV and > 100 eV populations in the ion line. A successful estimate of the cold ion density may require successful partitioning of the ion line counts between the two populations, which in turn could be used to better estimate the >100 eV ion moments in the presence of spacecraft charging.

6.3.4 Combined Partial Moments

As discussed above, there may be a desire to combine the partial moments from the three energy ranges produced by the algorithm. Partial moments can be combined as follows:

$$n = \sum_i n_i \tag{42}$$

$$T = \frac{\sum_i n_i T_i}{\sum_i n_i} \tag{43}$$

where i is the energy range. The second expression is derived from the observation that partial energy densities (nT, keV cm^{-3}) add, not temperatures.

7.0 REFERENCES

Baker, D. N. (1996), Solar wind-magnetosphere drivers of space weather, *J. Atmos. Terr. Phys.*, *58*, 1509-1526.

Bame, S. J., D. J. McComas, M. F. Thomsen, B. L. Barraclough, R. C. Elphic, J. P. Glore, J. T. Gosling, J. C. Chavez, E. P. Evans, and F. J. Wymer (1993), Magnetospheric plasma analyzer for spacecraft with constrained resources. *Rev. Sci. Instrum.*, *64*, 1026-1033.

Blum, L. W., E. A. MacDonald, S. P. Gary, M. F. Thomsen, and H. E. Spence (2009), Ion observations from geosynchronous orbit as a proxy for ion cyclotron wave growth during storm times, *J. Geophys. Res.*, *114*, A10214, doi:10.1029/2009JA014396.

Cayton, T. E., R. D. Belian, S. P. Gary, T. A. Fritz, and D. N. Baker (1989), Energetic electron components at geosynchronous orbit, *Geophys. Res. Lett.*, *16*, 147-150.

Chapman, S., and T. G. Cowling (1970), *The Mathematical Theory of Non-Uniform Gases*, Third Edition, 423 pp., Cambridge: Cambridge University Press.

Cubero, D., J. Casado-Pascual, J. Dunkel, P. Talkner, and P. Hänggi (2007), Thermal equilibrium and statistical thermometers in special relativity, *Phys. Rev. Lett.*, *99*, 170601.

Daglis, I. A., S. Livi, E. T. Sarris, and B. Wilken (1994), Energy density of ionospheric and solar wind origin ions in the near-Earth magnetotail during substorms, *J. Geophys. Res.*, *99*, 5691-5703.

DeForest, S. E. (1972), Spacecraft charging at synchronous orbit, *J. Geophys. Res.*, *77*, 651-659.

DeForest, S. E., and C. E. McIlwain (1971), Plasma clouds in the magnetosphere, *J. Geophys. Res.*, *76*, 3587-3611.

de Groot, S. R., W. A. van Leeuwen, and Ch. G. van Weert (1980), *Relativistic Kinetic Theory: Principles and Applications*, 417 pp., Amsterdam: North-Holland Publishing Company.

Erdélyi, A., et al. (1954), *Tables of Integral Transforms*, Volume 1, New York: McGraw-Hill Book Co.

Farthing, W. H., J. P. Brown, and W. C. Bryant (1982), Differential spacecraft charging on the Geostationary Operational Environmental Satellites, *NASA Tech. Mem. 83908*, 44 pp.

Fennell, J. F., et al. (2010), Charged deposition behind known shielding in a highly inclined orbit, 11th Spacecraft Charging Technology Conference, Albuquerque, New Mexico.

Garrett, H. B. (1981), The charging of spacecraft surfaces, *Rev. Geophys., 19,* 577-616.

Garrett, H. B., D. C. Schwank, P. R. Higbie, and D. N. Baker (1980), Comparison between the 30- to 80-keV electron channels on ATS 6 and 1976-059A during conjunction and application to spacecraft charging prediction, *J. Geophys. Res., 85,* 1155-1162.

Gradshteyn, I. S., and I. M. Ryzhik (1980), *Table of Integrals, Series and Products,* Corrected and Enlarged Edition prepared by A. Jeffrey, 1160 pp., Academic Press.

Gussenhoven, M. S., and E. G. Mullen (1983), Geosynchronous environment for severe spacecraft charging, *J. Spacecraft Rockets, 20,* 26-34.

Hartley, D. P., M. H. Denton, and J. V. Rodriguez (2014), Electron number density, temperature, and energy density at GEO and links to the solar wind: A simple predictive capability, *J. Geophys. Res. Space Physics, 119,* 4556–4571, doi:10.1002/2014JA019779.

Hill, T. W., and P. H. Reiff (1977), Evidence of magnetospheric cusp proton acceleration by magnetic merging at the dayside magnetopause, *J. Geophys. Res., 82,* 3623-3628.

Jüttner, F.(1911), Das Maxwellsche Gesetz der Geschwindigkeitsverteilung in der Relativtheorie, *Ann. Phys. (Leipzig), 34,* 856-882.

Kennel, C. F., and H. E. Petschek (1966), Limit on stably trapped particle fluxes, *J. Geophys. Res., 71,* 1-28.

Koons, H., J. Mazur, A. Lopatin, D. Pitchford, A. Bogorad, and R. Herschitz (2006), Spatial and temporal correlation of spacecraft surface charging in geosynchronous orbit, *J. Spacecraft Rockets, 43,* 178-185.

MacDonald, E. A., M. H. Denton, M. F. Thomsen, and S. P. Gary (2008), Superposed epoch analysis of a whistler instability criterion at geosynchronous orbit during geomagnetic storms, *J. Atmos. Solar-Terr. Phys., 70,* 1789-1796.

McComas, D. J., S. J. Bame, B. L. Barraclough, J. R. Donart, R. C. Elphic, J. T. Gosling, M. B. Moldwin, K. R. Moore, and M. F. Thomsen (1993), Magnetospheric Plasma Analyzer: Initial three-spacecraft observations from geosynchronous orbit, *J. Geophys. Res., 98,* 13,453-13,465.

McComas, D. J., R. C. Elphic, M. B. Moldwin, and M. F. Thomsen (1994), Plasma observations of magnetopause crossings at geosynchronous orbit, *J. Geophys. Res., 99,* 21,249-21,255.

McIlwain, C. E. (1972), Plasma convection in the vicinity of the geosynchronous orbit, in *Earth's Magnetospheric Processes*, pp. 268-279, B. M. McCormac, ed.

McIlwain, C. E., and E. C. Whipple (1986), The dynamic behavior of plasmas observed near geosynchronous orbit, *IEEE Trans. Plasma Sci., PS-14,* 874-890.

Newell, P. T., and C.-I. Meng (1988), The cusp and the cleft/boundary layer: low-altitude identifications and statistical local time variation, *J. Geophys. Res., 93*, 14549.

Newell, P. T., and C.-I. Meng (1995), Cusp low-energy ion cutoffs: A survey and implications for merging, *J. Geophys. Res., 100*, 21943.

O'Brien, P. (2010), Documentation of C Inversion Library, September 22, 2010. Available at: http://irbem.svn.sourceforge.net/viewvc/irbem/extras/invlib/doc/invlib.pdf

Olsen, R. C. (1986), Record charging events from Applied Technology Satellite 6, *J. Spacecraft, 24,* 362-366.

Onsager, T. G., A. A. Chan, Y. Fei, S. R. Elkington, J. C. Green, and H. J. Singer (2004), The radial gradient of relativistic electrons at geosynchronous orbit, *J. Geophys. Res., 109*, A05221, doi:10.1029/2003JA010368.

Roederer, J. G. (1970), *Dynamics of Geomagnetically Trapped Radiation*, 166 pp., New York: Springer-Verlag.

Synge, J. L. (1957), *The Relativistic Gas*, 108 pp., Amsterdam: North-Holland Publishing Company.

Thomsen, M. F., D. J. McComas, G. D. Reeves, and L. A. Weiss (1996), An observational test of the Tsyganenko (T89a) model of the magnetospheric field, *J. Geophys. Res., 101,* 24,827-24,836.

Thomsen, M. F., E. Noveroske, J. E. Borovsky, and D. J. McComas (1999), Calculation of moments from measurements by the Los Alamos magnetospheric plasma analyzer, LA-13566-MS.

Twomey, S. (1977), *Introduction to the Mathematics of Inversion in Remote Sensing and Indirect Measurements,* 243 pp., Mineola, NY: Dover.

Whipple, E. C., Jr. (1976), Observation of photoelectrons and secondary electrons reflected from a potential barrier in the vicinity of ATS 6, *J. Geophys. Res., 81,* 715-719.

APPENDIX A. OVERVIEW OF PARTICLE DISTRIBUTIONS

The calculation of moments involves particle fluxes and their conversion to velocity distributions or phase space densities. The purpose of this appendix is to provide a brief introduction to the subject for those unfamiliar with the subject, as well as a ready reference to various useful expressions. The conversions from one unit system to another are particularly helpful in the context of this algorithm.

The calibration of the MPS-LO and MPS-HI instruments enables the measured count rates to be converted to differential directional number fluxes, j, by the Level 1b algorithms. Ideally, such fluxes are differential in energy and in direction, though in practice the instruments average the measured fluxes over finite energy channels and angular zones. In the energy range covered by MPS-LO and MPS-HI, differential directional number fluxes are typically expressed in units of particles s^{-1} cm^{-2} sr^{-1} keV^{-1} (for example, see the SEISS PORD). We refer to this quantity simply as "differential flux" throughout this ATBD.

Velocity moments are calculated from particle velocity distributions in the non-relativistic limit. Therefore, we have to convert the measured differential fluxes to velocity distributions. For MPS-HI electrons, because a relativistic treatment is required, we need to use the equivalent momentum distribution or phase space density.

The phase space density is the ratio of the differential flux to the square of the momentum of the particles [*Roederer*, 1970, p. 89; *Onsager et al.*, 2004]:

$$F_p = \frac{j}{p^2} \tag{44}$$

The units of relativistic phase space density in this algorithm are keV^{-3} s^{-3}.

In the relativistic case, the momentum p of a particle is given by the expression

$$p = \gamma m_o v \tag{45}$$

where gamma is given by:

$$\gamma = \frac{1}{\sqrt{1 - v^2/c^2}} = 1 + \frac{E}{m_o c^2} \tag{46}$$

The momentum can be expressed therefore in terms of the kinetic energy as follows:

$$p^2 c^2 = E^2 + 2 m_o c^2 E \tag{47}$$

where c is the speed of light in vacuum, E is the kinetic energy of the particle, m_o is the rest mass and m_oc^2 is the rest energy of the particle.

The velocity distribution can be derived from the momentum phase space distribution relativistically as follows [*Synge*, 1957, p. 17]:

$$f_v = m_o^3 \gamma^5 F_p \tag{48}$$

Therefore, using the relativistic expression for momentum, the velocity distribution is related to the measured differential flux as follows:

$$f_v(\alpha_{k,} v_i) = \frac{m_o \gamma^3}{v_i^2} j(\alpha_{k,} E_i) \tag{49}$$

Since the kinetic energy is the independent variable in the measurements, the velocity in this expression has to be calculated relativistically as well:

$$v^2 = c^2 \left(1 - \frac{1}{\gamma^2}\right) \tag{50}$$

It is incorrect to use a relativistic velocity distribution in a non-relativistic moment integral. This results in a substantial overestimate of both density and temperature.

In the non-relativistic case, where E is much less than m_oc^2, $\gamma \approx 1$ and the velocity can be calculated from the kinetic energy as:

$$v^2 = \frac{2E}{m_o} \tag{51}$$

And, of course, the non-relativistic velocity distribution simplifies to:

$$f_v(\alpha_{k,} v_i) = \frac{m_o}{v_i^2} j(\alpha_{k,} E_i) \tag{52}$$

The units of the non-relativistic velocity distribution in this algorithm are $s^3\ cm^{-6}$.

An isotropic, non-relativistic Maxwellian velocity distribution with zero drift velocity is given by [*Chapman and Cowling*, 1970, p. 69]

$$f_v = n\left(\frac{m}{2\pi kT}\right)^{3/2} \exp\left(-\frac{E}{kT}\right) \tag{53}$$

A bi-Maxwellian distribution has different parallel and perpendicular temperatures [*Hill and Reiff*, 1977]:

$$f_v = n\left(\frac{m}{2\pi kT_{par}}\right)^{1/2}\left(\frac{m}{2\pi kT_{perp}}\right)\exp\left(-\frac{E\cos^2\alpha}{kT_{par}}\right)\exp\left(-\frac{E\sin^2\alpha}{kT_{perp}}\right) \tag{54}$$

The phase space density for a relativistic, isotropic Maxwellian distribution is given by [*Jüttner*, 1911; *Synge*, 1957, p. 36; *Cayton et al.*, 1989; *Cubero et al.*, 2007]:

$$F_p = \frac{nc}{4\pi m_o (kT)^2}\frac{1}{\beta\exp(\beta)K_2(\beta)}\exp\left(-\frac{E}{kT}\right) \tag{55}$$

where E is the kinetic energy of the particle, m_o is the rest mass, n is the number density, c is the speed of light, T is the temperature, k is Boltzmann's constant, and β is the rest mass (in energy units) divided by kT:

$$\beta = \frac{m_o c^2}{kT} \tag{56}$$

K_2 is the modified Bessel function of the second kind of order 2.

APPENDIX B. EVALUATION OF MOMENTS FOR MAXWELLIAN DISTRIBUTIONS

The purpose of this appendix is to show that the moment integrals give number density and temperature for a Maxwellian distribution. For simplicity, we just treat the isotropic case.

For the non-relativistic case, the density and temperature of an isotropic distribution are given by:

$$n = 4\pi\int f_v(v)v^2 dv \tag{57}$$

$$kT = \frac{4\pi m}{3n}\int f_v(v)v^4 dv \tag{58}$$

The Maxwellian velocity distribution is given by:

$$f_v = n\left(\frac{m}{2\pi kT}\right)^{3/2}\exp\left(-\frac{E}{kT}\right) \tag{59}$$

The following definite integral [*Gradshteyn and Ryzhik*, 1980, 3.461 2] can be used to solve for both n and T:

$$\int_0^\infty x^{2n} \exp\left(-ax^2\right)dx = \frac{(2n-1)!!}{2(2a)^n}\sqrt{\frac{\pi}{a}} \tag{60}$$

$$\int_0^\infty v^2 \exp\left(-\frac{mv^2}{2kT}\right)dv = \sqrt{\frac{\pi}{2}}\left(\frac{kT}{m}\right)^{3/2} \tag{61}$$

$$\int_0^\infty v^4 \exp\left(-\frac{mv^2}{2kT}\right)dv = 3\sqrt{\frac{\pi}{2}}\left(\frac{kT}{m}\right)^{5/2} \tag{62}$$

With these identities, it is straightforward to show that the zeroth and second velocity moments give number density and temperature, respectively.

In the relativistic case, the density of an isotropic distribution is given by

$$n = 4\pi \int F_p(\alpha, p) p^2 dp \tag{63}$$

and the distribution-weighted energy from which temperature is derived is given by

$$E_T = \frac{8\pi}{3n}\int E F_p(\alpha, p) p^2\, dp \tag{64}$$

The relativistic Maxwellian phase space density is given by:

$$F_p = \frac{nc}{4\pi m_o (kT)^2}\frac{1}{\beta \exp(\beta) K_2(\beta)}\exp\left(-\frac{E}{kT}\right) \tag{65}$$

As a function of momentum and rest mass, kinetic energy is given by:

$$E = \sqrt{\left(m_o c^2\right)^2 + p^2 c^2} - m_o c^2 \tag{66}$$

By making the following change of variables,

$$p^2 = a^2\left(x^2 - 1\right) \tag{67}$$

the number density and energy integrals (omitting constants in front) can be rewritten as

$$\int p^2 \exp\left(\frac{-E}{kT}\right)dp = a^3 \exp(\beta)\int x\left(x^2-1\right)^{1/2}\exp(-\beta x)dx \tag{68}$$

$$\int Ep^2 \exp\left(\frac{-E}{kT}\right)dp = ca^4 \exp(\beta)\left\{\int x^2\left(x^2-1\right)^{1/2}\exp(-\beta x)dx - \int x\left(x^2-1\right)^{1/2}\exp(-\beta x)dx\right\} \tag{69}$$

where $a = m_o c$ and $\beta = m_o c^2/(kT)$.

It can be seen that these are Laplace transforms. The following transform [*Erdélyi et al.*, 1954, p. 138, eqn. 11],

$$\int_0^\infty \left(x^2-b^2\right)^{\nu-1/2}\exp(-sx)dx = \frac{\Gamma\left(\nu+\frac{1}{2}\right)}{\pi^{1/2}}\left(\frac{2b}{s}\right)^\nu K_\nu(as) \tag{70}$$

(where K_ν is the modified Bessel function of the second kind of order ν), combined with the property of Laplace transform pairs {f(x), g(s)} that

$$x^n f(x) \rightarrow (-1)^n \frac{\partial^n g(s)}{\partial s^n} \tag{71}$$

can be used to solve the above integrals. (Recurrence formulas for modified Bessel functions of the second kind and their derivatives are employed in this solution.) The result confirms that the relativistic number density integral stated above indeed gives the correct number density, and that the integral E_T for a relativistic Maxwellian distribution gives

$$E_T = \frac{2}{3}m_o c^2\left[\frac{K_1(\beta)}{K_2(\beta)}+\frac{3}{\beta}-1\right] \tag{72}$$

To find the expression for E_T in the non-relativistic limit, one takes the asymptotic expansions of large argument for modified Bessel functions of the second kind (large β corresponds to $kT << m_o c^2$).

$$K_1(\beta) \sim \sqrt{\frac{\pi}{2\beta}}\exp(-\beta)\left(1+\frac{3}{8\beta}+\ldots\right) \tag{73}$$

$$K_2(\beta) \sim \sqrt{\frac{\pi}{2\beta}}\exp(-\beta)\left(1+\frac{15}{8\beta}+\ldots\right) \tag{74}$$

To get the correct result, the second term in the expansions must be included. Applying the binomial expansion theorem, the result in the non-relativistic limit is that $E_T = kT$. See Figure 6 for a comparison of the relativistic and non-relativistic forms as a function of β.

APPENDIX C. DERIVATION OF MOMENTUM TERMS IN RELATIVISTIC TEMPERATURE SOLUTION

Taking the isotropic case for simplicity of presentation, the relativistic temperature integral is approximated as

$$E_T = \frac{8\pi}{3n}\int EF_p(\alpha, p)p^2\,dp \approx \frac{8\pi}{3n}\sum_{i=0}^{N_{ch}-1} F_p(p_i)\int_{p_{i,\min}}^{p_{i,\max}}\left(\sqrt{(m_o c^2)^2 + p^2c^2} - m_o c^2\right)p^2 dp \qquad (75)$$

The momentum term is the difference of two integrals, the second of which is straightforward to solve. The solution of the first integral can be found in *Gradshteyn and Ryzhik* [1980, 2.272 1]:

$$\int x^2\left(a+bx^2\right)^{1/2}dx = \frac{1}{4}\frac{x\left(a+bx^2\right)^{3/2}}{b} - \frac{1}{8}\frac{ax\left(a+bx^2\right)^{1/2}}{b} - \frac{1}{8}\frac{a^2}{b^{3/2}}\ln\left[b^{1/2}x + \left(a+bx^2\right)^{1/2}\right] \qquad (76)$$

Therefore, after some manipulation, the indefinite integral to be evaluated at the limits of the momentum bin is given by

$$\begin{aligned} h(p) &= \int\left(\sqrt{(m_o c^2)^2 + p^2c^2} - m_o c^2\right)p^2 dp = \\ &\frac{p}{4c^2}\left[(m_o c^2)^2 + p^2c^2\right]^{\frac{3}{2}} - \frac{1}{8}(m_o c^2)^2\frac{p}{c^2}\left[(m_o c^2)^2 + p^2c^2\right]^{\frac{1}{2}} \\ &-\frac{1}{8}(m_o c^2)^4\frac{1}{c^3}\ln\left\{cp + \left[(m_o c^2)^2 + p^2c^2\right]^{\frac{1}{2}}\right\} - \frac{1}{3}m_o c^2 p^3 \end{aligned} \qquad (77)$$

This expression has units keV^4 s^3 cm^{-3}. The groupings of the rest mass $m_o c^2$ (expressed in keV), along with p in keV s cm^{-1} and c in cm s^{-1}, are intended to make the units conversion straightforward in the temperature computation